heritage

MDPI

Article

Three-Dimensional Digital Documentation for the Conservation of the Prambanan Temple Cluster Using Guided Multi-Sensor Techniques

Anindya Sricandra Prasidya [1,2], Irwan Gumilar [3,*], Irwan Meilano [4], Ikaputra Ikaputra [5], Rochmad Muryamto [2] and Erlyna Nour Arrofiqoh [2]

[1] Department of Geodesy and Geomatics Engineering, Faculty of Earth Sciences and Technology, Institut Teknologi Bandung, Jalan Ganesha 10, Bandung 40132, Indonesia; 35121005@mahasiswa.itb.ac.id
[2] Department of Earth Technology, Vocational College, Gadjah Mada Univeristy, Jalan C Simanjuntak 76A, Yogyakarta 55281, Indonesia; rochmad_mury@ugm.ac.id (R.M.); erlyna_na@ugm.ac.id (E.N.A.)
[3] Geodetic Science, Engineering, and Innovation Research Group, Faculty of Earth Sciences and Technology, Institut Teknologi Bandung, Jalan Ganesha 10, Bandung 40132, Indonesia
[4] Spatial System and Cadastre Research Group, Faculty of Earth Sciences and Technology, Institut Teknologi Bandung, Jalan Ganesha 10, Bandung 40132, Indonesia; irwanm@itb.ac.id
[5] Department of Architecture and Planning, Faculty of Engineering, Gadjah Mada Univeristy, Jalan Grafika 02, Yogyakarta 55284, Indonesia; ikaputra@ugm.ac.id
* Correspondence: igumilar@itb.ac.id

Abstract: The Prambanan Temple cluster is a world heritage site that has significant value for humanity, a multiple zone cluster arrangement of highly ornamented towering temples, and a Hindu architectural pattern design. It lies near the Opak Fault, at the foothills of Mount Merapi, on an unstable ground layer, and is surrounded by human activities in Yogyakarta, Indonesia. The site's vulnerability implies the necessity of 3D digital documentation for its conservation, but its complexity poses difficulties. This work aimed to address this challenge by introducing the utilization of architectural pattern design (APD) to guide multi-sensor line-ups for documentation. First, APDs were established from the literature to derive the associated multiple detail levels; then, multiple sensors and modes of light detection and ranging (Lidar) scanners and photogrammetry were utilized according to their detail requirements and, finally, point cloud data were processed, integrated, assessed, and validated by the proof of the existence of an APD. The internal and external qualities of each sensor result showed the millimeter- to centimeter-range root mean squared error, with the terrestrial laser scanner (TLS) having the best accuracy, followed by aerial close-range and terrestrial-mode photogrammetry and nadiral Lidar and photogrammetry. Two relative cloud distance analyses of every point cloud model to the reference model (TLS) returned the millimeter and centimeter ranges of the mean distance values. Furthermore, visually, every point cloud model from each sensor successfully complemented each other. Therefore, we can conclude that our approach is promising for complex heritage documentation. These results provide a solid foundation for future analyses, particularly in assessing structural vulnerabilities and informing conservation strategies.

Keywords: the Prambanan temples; multi-sensor; architectural pattern design; Lidar; photogrammetry

Academic Editors: George Alexis Ioannakis and Anestis Koutsoudis

Received: 26 November 2024
Revised: 30 December 2024
Accepted: 3 January 2025
Published: 16 January 2025

Citation: Prasidya, A.S.; Gumilar, I.; Meilano, I.; Ikaputra, I.; Muryamto, R.; Arrofiqoh, E.N. Three-Dimensional Digital Documentation for the Conservation of the Prambanan Temple Cluster Using Guided Multi-Sensor Techniques. *Heritage* **2025**, *8*, 32. https://doi.org/10.3390/heritage8010032

1. Introduction

The Prambanan Temple complex is one of the largest Hindu temples in the world and is located in Yogyakarta, Indonesia (see Figure 1) [1,2]. According to a Sivargrha inscription, it was reportedly built around the 9th century AD (832–856 AD) by Rakai Pikatan and was officiated by Rakai Kayuwangi during the glory days of Sanjaya's powerful reign [3–5]. It has been officially listed as a UNESCO World Heritage site since 1991 [1,6]. This cultural heritage (CH) reveals the advancement of ancient human knowledge and skills for the planning and construction of well-arranged monuments, both physically and philosophically [7–9]. It also depicts traditional construction techniques that represent local wisdom, which are called interlocking stone techniques [9]. The temple was constructed using stone masonry procedures by applying Mahameru and Tripartite concepts, resulting in a towering temple with a triangle-shaped silhouette from its base (Bhurloka), body (Bhuvarloka), and head (Svarloka) [8]. The temple façade was then decorated with well-arranged elements, ornaments, moldings, carvings, and narrative bas-reliefs, which depict symbolic representations of Hindu philosophy and cultural values [7,8]. The temple was then clustered in the core zone, buffer zone, and development zone [2,10] based on its degree of importance and staging. In the core zone, there are three main temples dedicated to Trimurti figures of worship—Shiva (the Creator), Vishnu (the Preserver), and Brahma (the Destroyer)—and three temples dedicated to their mounts (vehicles): Garuda (mount of Vishnu), Nandhi (mount of Shiva), and Hamsha (mount of Brahma). The other temples are Apit (north and south, to distinguish Trimurti and their mounts), Kelir (four temples at each entrance gate, parallel to the main cardinal direction), and Patok (four temples at each corner) [2,4,6,10]. See Figure 1 for details. In the buffer zone, there are 244 Perwara Temples that are arranged in a concentric and symmetrical layout and expand from the core zone [4]. In the outermost zone, there is a supporting courtyard of the temple complex, which is mainly used for tourism purposes [11]. This entire arrangement is not arbitrary but follows certain rules and patterns of composition [2,7,8,12]. It enhances the cultural and architectural significance of the Prambanan Temple.

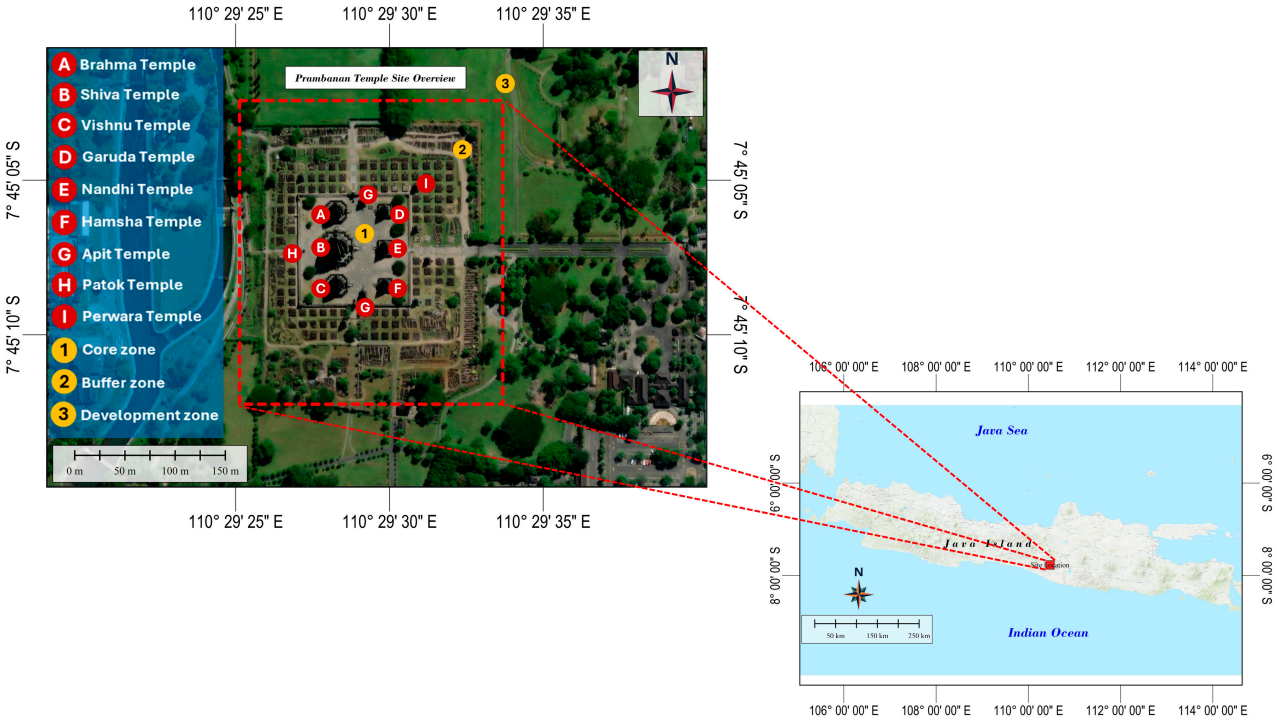

Figure 1. The Prambanan Temple cluster's location and its concentric layout arrangement.

Architectural design attributes in the Prambanan Temple are among the topics discussed by researchers in [7,13–15]. The Prambanan Temple is believed to be architecturally similar to another Hindu temple, Angkor Wat, in Cambodia [14], and the Lingaraja Temple in India [13]. Herwindo [7,8] stated that it most likely followed a set of plans and construction principles from the Manasara book (from South India). This assumption was based on the similarities in Prambanan Temple sites with a set of principles from the Manasara book: close proximity to water sources, soil layer type of foundation, land works, façade type, utilization of Mandala as a basis, spatial typology and morphology, etc. [7]. The Prambanan Temple was not only tied to a religious temple style and fully followed the Manasara book, but it was also a combination of religious and local Javanese wisdom [8] because some Javanese temples, both Hindu and Buddhist, from the same era had the same characteristics [14]. At this point, 11 architectural design attributes have been revealed by [7] based on (a) several points of view of Mandala design and (b) the comparisons between the Prambanan Temple and Sewu Temple (same era (9th century) and area). Furthermore, Mandala or Vasthu Purusha Mandala rules are believed to be the reason behind the design of most Hindu temples [13,15,16], including the Prambanan Temple [7]. In addition, the Prambanan Temple also proved that its layout was well-planned using astronomical knowledge [2] and the fractal geometry concept [15]. Based on the above literature, the debate on the architectural design of the Prambanan Temple is only about which references and which design principles were more likely adopted during the planning and construction time.

Aside from the significance of the Prambanan Temple, it is now facing several problems. Geographically, it is located near the Opak fault zones [6,17], on the foothills of the Merapi volcano [18], in a tropical urban area [18], on an unstable clay and sand soil foundation [19], and in a famous tourism site [1]. These situations make it vulnerable to numerous threats, such as earthquakes, ground motion, eruptions, weather disturbances, pollution, and vandalism [18]. These threats could disturb the integrity and existence of the temple, causing damage and even collapse at some point. For example, the 5.6 Mw near-surface earthquake on 26 May 2006, originating from the Opak fault, struck Yogyakarta [20,21] and caused extensive damage to the Prambanan Temple, including material loss, cracks, fractures, spallings, and deformations [6], and submerged the foundations of several temples [19]. This implies that related stakeholders should prioritize the preservation of this cultural heritage; otherwise, future generations may no longer have the chance to witness this outstanding monument. Generally, preservation should begin with proper documentation and a 3D modeling process [22].

The documentation of cultural heritage is related to tangible and intangible information acquisition and storage [23], which can be conducted manually or digitally. Due to the requirements to maintain its existence, the tangible aspect should be prioritized without overlooking other aspects. Geometry documentation is an implementation of the tangible aspect. It is known as 2D or 3D data collection, which utilizes several measuring techniques to completely represent the shape, size, dimension, and orientation of an object of interest. The product is most likely in the form of 2D drawings, a 3D digital model, or a more advanced BIM model. It helps stakeholders to plan and execute conservation and restoration [24–27]. Damage to a cultural heritage site can now be handled by implementing 3D documentation as a basis for the decision-making process.

Heritage 3D documentation usually starts with measurements. Several sensors can be utilized. Generally, it can be classified as range-based and image-based [28,29] for both low- and high-density data types [30]. Low-density sensors, such as theodolite, total station, automatic level, and GNSS, commonly produce a set of 1D to 3D coordinates of a limited number of selected features [31,32]. They primarily serve as control point providers

and recorders of various geometric elements of CH [23,26,33]. In contrast, high-density sensors, which are widely favored sensors for heritage documentation [28,34], generate massive 3D data of objects from all visible angles in a particular resolution setting at a single recording. Examples of this type of instrument are Lidar sensors on various platforms (aerial, terrestrial, mobile, and handheld) [35,36]; cameras in various modes (frame, fisheye, spherical, and video) and various platforms (drone and terrestrial); and integrated real-time sensor systems such as the Mobile Mapping System (MMS). Each of the mentioned types of sensors has its own advantages and limitations, mostly due to data density, coverage, field of view, automation, portability, flexibility (real-time vs. static), usability, costs, etc. One sensor may not be the best at all of those aspects. Some are best at coverage, field of view, and data density only but not at portability, or they are best at data density and automation but not at coverage and cost. This is why one sensor with a single mode of measurement is incapable of completely measuring a complex shape. Therefore, multi-sensor systems are required to handle such problems.

Three-dimensional digital documentation has been widely implemented for modeling the characteristics of numerous heritage sites, such as buildings (office/house/church/palace) [26,37–40], monuments [41,42], fortresses [43,44], heritage ruins [45], landscapes with sparse heritage objects [29,46–48], etc. Landscapes with heritage objects have been documented in many ways. As mentioned by [46], the utilization of Lidar and unmanned aerial vehicle (UAV) ortho- and oblique sensors in a hierarchical approach (from landscape to structures and stratigraphy) could handle the 3D modeling process of large Treblinka archaeological sites, which mainly consist of building debris due to the genocide at that time. A similar approach was also applied at the urban CH complex, Kasepuhan Palace, Indonesia, but it was focused on the landscape, building, and moldings [29]. In other cases, UAV nadiral and oblique combined with terrestrial instruments have successfully documented the topographic and architectural parts (including wall condition) of an old castle–fortress building located at the top of a hill (Scalea, Italy) [48].

Based on the literature [29,46,48], multi-sensor approaches were recommended with or without multiscale manners for various kinds of architectural heritage. However, none of these studies mentioned the basis for the selected approaches. Furthermore, none were interested in extending the existing approaches to the towering, highly decorated temple cluster in a concentric layout landscape, like the Prambanan Temple. In fact, some of the CH sites were built by following a certain philosophy, which makes them have certain design attributes as well. Therefore, extending the current approaches to the towering, highly decorated temple cluster driven by their design attributes must be prioritized.

In Indonesia, similar 3D digital heritage documentation has been applied to many cultural heritage monuments, buildings, sites, and regions. These include, for example, the Borobudur Temple [49,50], Sewu Temple [47], Ijo Temple [51], Sari Temple [52], Kasepuhan Palace [29], some heritage buildings in Malang [53], Vrederburg Fortress, Kotagede Mosque at Yogyakarta [43], and so forth. Some used multiple sensors, while others used a single sensor. However, compared to other cultural heritage sites, the Prambanan Temple has its own characteristics, which consist of individual temple groups in concentric squared zones and multiple geometric information types: topographic, façade geometry, structural support, building elements, moldings, ornaments, reliefs, carvings, etc. All of this information has equal integrity and contains intangible values. In short, every part of the temple has its own inherent value. The temple itself was built by following Hindu philosophy, which was implemented in the temple design, layout, and arrangement, both individually and in groups. A lack of information may result in incomplete depictions of temples, both geometrically and philosophically. We may lose complete descriptions of temples. That is why every single type of information is important.

This study aims to propose a technique for documenting the geometric aspect of highly decorated and towering concentric temple clusters (TCTCs). The technique involves the utilization of multiple sensor recordings at different scales, guided by their design attributes. This paper is organized into five sections. Section 1 discusses the motivation and the recent works regarding documentation around the world, particularly in Indonesia. Section 2 discusses the proposed methodology. Sections 3 and 4 present the results and provide a discussion, respectively, followed by Section 5, which mentions the conclusion and future outlook.

2. Methodology

2.1. Materials and Methods

Several sensors, epochs, and scales have been used to deal with the complexity of Prambanan Temple site settings, including UAV-Lidar, TLS, nadiral UAV photogrammetry, close-range UAV photogrammetry (CR-UAVP), terrestrial frame photogrammetry, terrestrial spherical photogrammetry, and low-cost Lidar sensors. The specification of each acquired data type is summarized in Table 1.

Table 1. Summary of utilized sensors and their coverage in the TCTC case.

						Main Temple Coverage *					
No	**Data Types**	**Year**	**Instrument/Sensor**	**Specification**	**Measurement Target**	**H**	**B**	**G**	**N**	**S**	**V**
1	Nadiral aerial photographs	2020	42.4 MP camera installed on UAV-copter Microdrones md1000DG	Image resolution: 42.4 Mega pixel	The 1st and 2nd courtyard landscapes	✓	✓	✓	✓	✓	#
2	Aerial Lidar point clouds	2020	Lidar sensor embedded on UAV-copter Microdrones mdLiDAR-1000DG	Density: 47 points/m^2, System accuracy of Lidar pointcloud: 6 cm vertical and 6 cm horizontal	The 1st and 2nd courtyard landscapes	✓	✓	✓	✓	✓	#
3	TLS point clouds #1	2020	Terrestrial Laser Scanner Topcon GLS-2000	Density: 6.3 mm/10 m of distance (detail mode) or 12.5 mm/10 m of distance (standard mode); Measuring range modes: 130 m (short)/350 m (medium)/500 m (long); Direct-georeferencing capabilities; Integrated camera available	General façade and detailed façade of the 1st courtyard	✓	✓	✓	✓	✓	#
4	TLS point clouds #2	2023				✓	✓	✓	✓	✓	✓
5	CR-UAVP photographs #1	2020	20 MP camera installed on UAV-Copter DJI Phantom 4	Image resolution: 20 Mega pixel	Detailed façade of Shiva and Garuda Temples (upper and middle part)					✓	
7	Terrestrial photographs	2023	Mirrorless frame camera (Sony A6000 24 MP)	Image resolution: 24.3 Mega pixel; sensor type: CMOS APS-C HD	Detailed bas-relief at temple base of Hamsa, Brahma, Nandhi, and Vishnu Temples	✓	✓		✓		✓
8	CR-UAVP photographs #2	2023	20 MP camera installed on UAV-copter DJI Air S	Image resolution: 24 Mega pixel	Detailed façade of Hamsa, Brahma, Nandhi, and Vishnu Temples (upper and middle part)	✓	✓		✓		✓
9	Spherical 360° photographs	2023	Ricoh Theta S spherical camera	1/2.3″ 12MP CMOS sensor; F2.0 360° lens	Detailed bas-relief at temple base	✓	✓	✓	✓		✓
10	Low-cost Lidar point clouds	2023	Ipad Pro 2020 Lidar	Solid state lidar (not confidentially mentioned)		✓	✓	✓	✓		✓
11	Ground and Façade Deformation Control Point (GDCP and FDCP)	2020 and 2022	Geodetic GNSS static mode of 3 D.O.Y and 8 h observation	Signal capabilities: Double/multi-frequency signals, multi-constellation satellites tracking (GPS, BeiDou GLONASS, GALILEO, QZSS), RINEX v2 v3 logging	Establishment of geometric control at façade and ground in the 1st courtyard	✓	✓	✓	✓	✓	✓
12	Dimension and points for independent checking	2021 and 2023	RTK GNSS (Base at S001) ComNav T300 receiver, measuring tape, and as-built drawing	RTCM2x/3x/CMR/CMR+ real-time correction, WiFi/UHF/4G modem connection, RTK horizontal accuracy: 8 mm + 1 ppm, vertical accuracy: 15mm + 1 ppm	Provides geometric quality check data	✓	✓	✓	✓	✓	✓

* Symbol: H = Hamsa, B = Brahma, G = Garuda, N = Nandhi, S = Shiva, V = Vishnu, ✓ = available, and # = under renovation.

To deal with the complexity of highly decorated, towering temple clusters, a workflow directed by architectural design attributes is proposed, as shown in Figure 2.

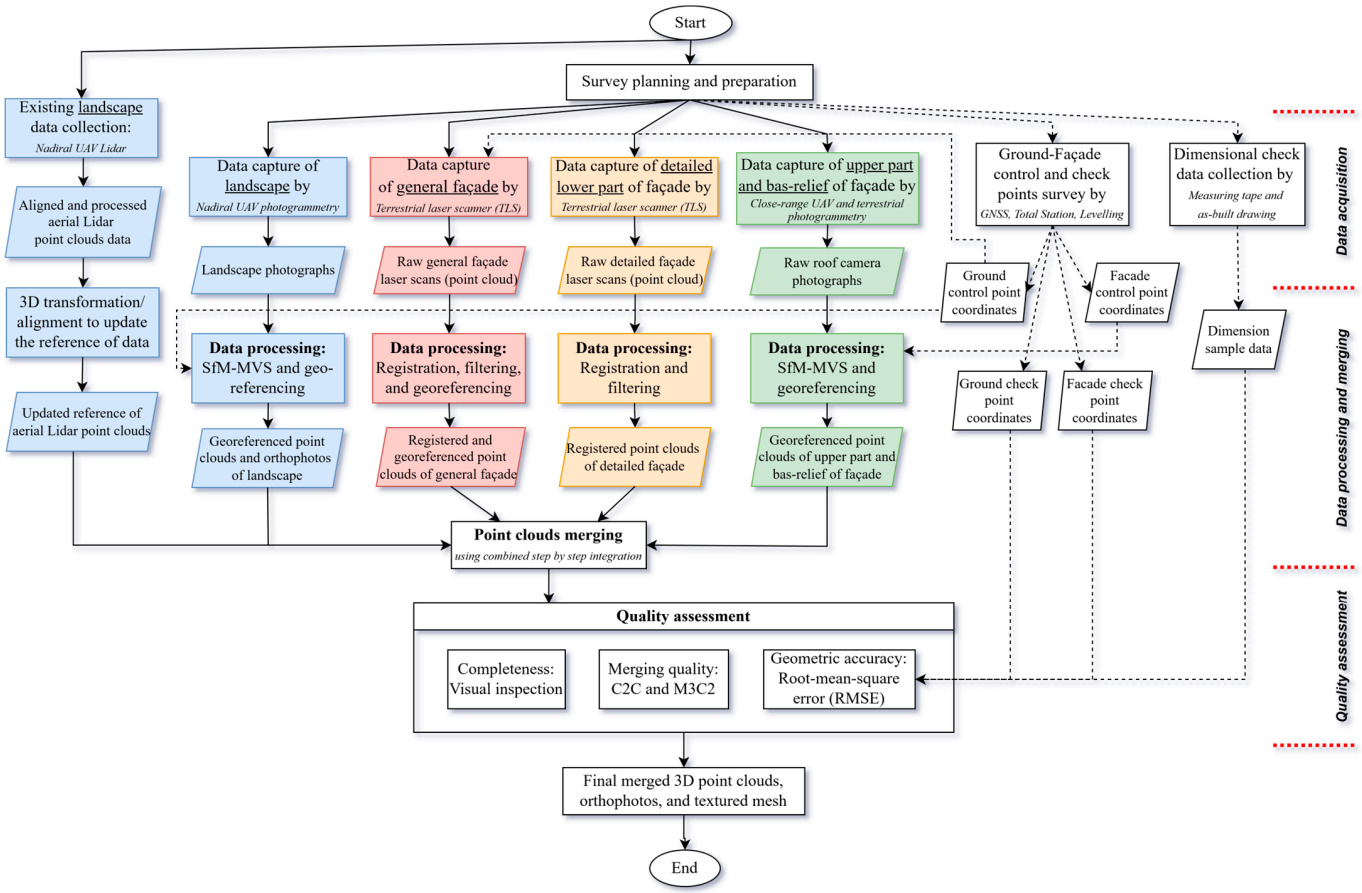

Figure 2. The proposed workflow. Solid arrows represent the main data flow, while the dashed arrows represent the supporting data flow.

This research leverages architectural design attributes (see Table 2) to develop a concept for CH data acquisition. The first step is to identify the literature mentioning architectural design attributes at the Prambanan Temple. Here, the architectural design attributes, or those mentioned earlier as APDs, are referred to as the revealed architectural attributes that are believed to be the underlying design aspect of the Hindu monument. The authors of [16,54] believed that the "Vasthu Purusha Mandala" in Vedas old scripture was the most famous concept to explain how the Prambanan Temples were built. It used the squared symmetrical design, incorporating a precise definition of ancient compass directions [8,13,16]. The cardinal direction concept was then proved to follow a certain astronomical calculation, not an arbitrary direction concept [2]. The researchers in [7] identified 11 architectural design attributes of the Prambanan Temple complex, providing the most detailed local literature on the subject. These attributes have high similarities to those found in the Angkor Wat Temple in Cambodia, which was built two centuries later [14]. Lastly, the fractal geometry concept was also used to describe the design of the Prambanan Temple algorithmically [15]. All of these studies are summarized in Table 2 to develop the concept of data acquisition for symmetrical concentric temple clusters (see Figure 3).

Table 2. Architectural design attributes and selected suitable sensors.

No	Architectural Design Attributes	Literature	Detail Level Categorization	Detail Level Requirement	Selected Suitable Sensor
1	Virtual embedded axis	[2,7,13,16]	Landscape level	Map scale of 1:1000	Nadiral UAV photogrammetry and Lidar
2	Hierarchical concept	[7,8]	Landscape level	Map scale of 1:1000	Nadiral UAV photogrammetry and Lidar
3	Clustered solid–void arrangement	[7,8]	Landscape level	Map scale of 1:1000	Nadiral UAV photogrammetry and Lidar
4	Multiple zoning of concentric courtyard	[4,9,10,18]	Landscape level	Map scale of 1:1000	Nadiral UAV photogrammetry and Lidar
5	Symmetrical arrangement	[7]	General and detailed façade	0.1 m of object details	Terrestrial Lidar scanner (TLS), close-range UAV photogrammetry
6	Rhythm and repetition	[7]	General and detailed façade	0.1 m of object details	Terrestrial Lidar scanner (TLS), close-range UAV photogrammetry
7	Scale and proportion	[7,12]	General and detailed façade	0.1 m of object details	Terrestrial Lidar scanner (TLS), close-range UAV photogrammetry
8	Tripartite concept	[7]	General and detailed façade	0.1 m of object details	Terrestrial Lidar scanner (TLS), close-range UAV photogrammetry
9	Mimesis concept	[7]	Detailed bas-relief	0.05 m	Terrestrial photogrammetry (frame)
10	Texture aspect	[7]	Detailed bas-relief	0.05 m	Terrestrial photogrammetry (frame)
11	Balanced ornament	[7]	Detailed bas-relief	0.05 m	Terrestrial photogrammetry (frame)
12	Decorated corridor	Authors' observation	Detailed bas-relief	0.05 m	Terrestrial photogrammetry (spherical)

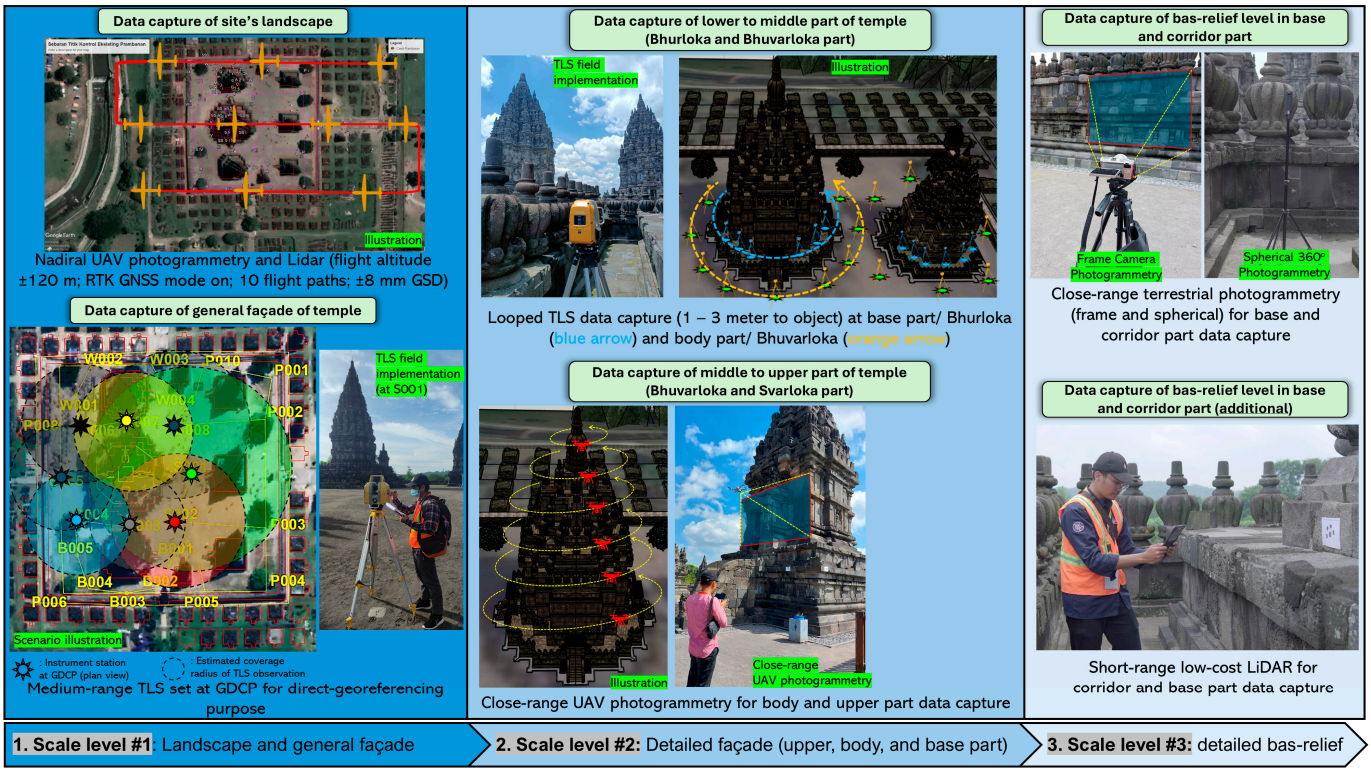

Figure 3. Data acquisition concept for three different scale levels. Darker colors represent larger scale levels, while lighter colors represent smaller scale levels. Google Earth and SketchUp 3D Warehouse provide background images for the left and center illustrations, respectively.

Based on the data acquisition concept (Figure 3), the multi-sensor concept was developed to handle multiple levels of CH detail. The detail level was established by considering several of the design attributes mentioned in Table 2. The first level of detail contains the landscape and general façade of all temple clusters in the main courtyard. This establishment comes from the fact that the temples have a virtual embedded axis, a hierarchical

concept, and a clustered solid–void arrangement. The second level of detail is the detailed façade that focuses on individual temple figures. This establishment comes from the fact that a temple designer cares about the symmetric arrangement aspect of a temple, as well as rhythm and repetition, utilizing scale and proportions, and using them in a triple-part temple division called *tripartite*. The third level of details is called the ornament and bas-relief level, which comes from the Mimesis concept, texture aspect, balanced ornament, and rhythm and repetition of the temple. The Mimesis concept itself is the sculptural representation of heavenly beings and deities when temporarily visiting and residing on the earth [8].

2.2. Data Acquisition for Geometric Control and Check

Two types of geometry control points located on the ground (called the ground deformation control point (GDCP)) and façade (called the façade deformation control point (FDCP)) that are mainly used for monitoring deformation phenomena were used in this study. GDCPs were established in 1999 in the form of concrete ground pillars that were distributed in the main courtyard only (Figure 4a) for conventional terrestrial deformation monitoring using theodolite and/or EDM [55,56]. They were then densified in 2018 and located on the second and third layers of a concentric courtyard to accommodate deformation monitoring using an extraterrestrial GNSS system [17] (see Figure 4a). The 3D coordinates of the GDCPs are now established by 3 day-of-year GNSS measurements for its primary network and 8 h of observation for its secondary network, which was repeated for 2 different epochs (2018 and 2020) and a global IGS station as a reference. It then produced 3D Cartesian coordinates (X, Y, Z) with coordinate standard deviations ranging from 8.95 mm to 77.87 mm (X component), 17.18 mm to 55.54 mm (Y component), and 43.73 mm to 9.52 mm (Z component). The orthometric height component of the GDCPs was measured by geometric leveling using the digital level that used the national vertical control station (TTG-856) as a reference datum [57]. The standard deviation of the height component was 1.35 mm to 1.58 mm. On the other hand, FDCPs were established simultaneously with GDCP densification in 2018 in the form of 19 permanently installed prisms in each direction of the main temple façade (see Figure 4b) [17]. It was measured by 3D coordinate triangulation using a Total Station instrument and a GDCP as a reference station [58]. The final coordinates were in horizontal UTM coordinates (northing, easting) with standard deviations ranging from 0.4 mm to 5.3 mm and vertical orthometric height coordinates (H) with standard deviations ranging from 1.2 mm to 8.4 mm. The same approach was performed in this study to establish additional coded targets to densify control points at the temple façade. These points were used to control and check the geometry of multi-source 3D data.

2.3. Data Acquisition for the Geometry of the Main Temple

As an implementation for the data acquisition concept (Figure 3), multi-mode photogrammetry and multi-platform Lidar were used as the primary 3D data scanner. It was controlled and checked by GDCPs and FDCPs, as well as temporary coded targets. The use of those sensors for multiple levels of CH detail 3D mapping was arranged according to its architectural design attributes.

To map the planar topography of the towering concentric temple cluster (TCTC) (1st level of CH detail), a nadiral drone Lidar scanner and nadiral drone photogrammetry were utilized. The flight mission simultaneously obtained both observations by setting the Microdrones md1000DG platform (carrying a 42.4 MP camera and Lidar sensor, respectively) to fly 120 m above the ground along 10 flight paths, on 8 mm of Ground Spatial Distance (GSD), in the RTK GNSS positioning mode, and with 60% overlap and 40% sidelap, hypo-

thetically [59]. The flight was performed under the requirement and permission of the CH management in October 2020.

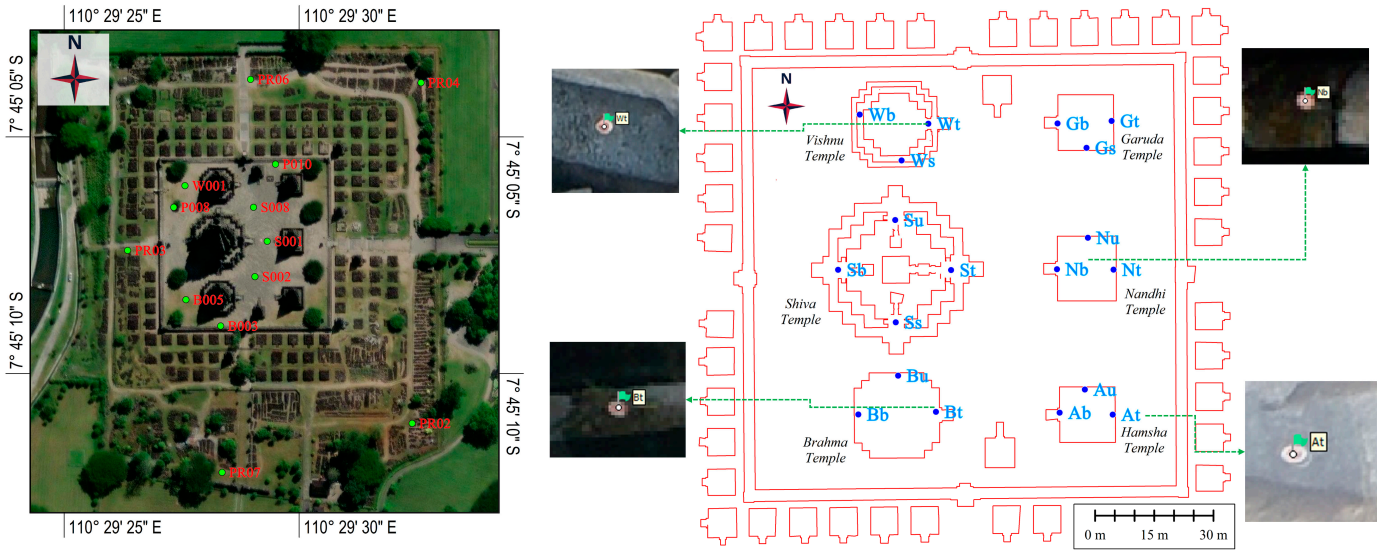

(**a**) (**b**)

Figure 4. Distribution of GDCPs (**a**) and FDCPs (**b**).

The object or perpendicular geometry of the TCTC (2nd level of CH detail) was mapped using close-range UAV photogrammetry (upper part of the TCTC), a terrestrial laser scanner (TLS) (bottom and middle part of the TCTC), and terrestrial photogrammetry using a frame camera (bottom and corridor part of the TCTC). Many successful works that utilized close-range UAV photogrammetry (CR-UAVP) to model towering buildings [41,60–63] inspired the authors to apply it to this TCTC case. The DJI Air S platform in free pilot mode was employed to take photographs circling around objects from a 5 to 10 m distance and gradually lower the flying altitude from the top of the towering temple to the ground (see Figure 3). In this case, the automatic flight using GPS guidance was intentionally avoided due to the high multipath from the site, low reception of the GPS signal, high obstruction (from the towering temple), and high mask angle, which may increase the risk of damaging the CH and compromise platform safety if the platform is out of control. The flight missions were performed sequentially on every temple in the main courtyard on the sterilized site day (each Monday) under the permission of the site's authorities in June 2023. On the other hand, the TLS is well-known as the most efficient sensor for 3D reality-based CH documentation [23]. For its implementation, a medium-range TLS type, Topcon GLS-2000, was used to scan up to 350 m for two point density options, i.e., 6 mm per 10 m distance (detailed mode—up to 100 m) or 12.5 mm per 10 m (standard mode), with an ability to perform both free-stationing and fixed-stationing (direct georeferencing) (Topcon GLS-2000 Manual). The TLS was set in a total of 79 scan stations in both free-station and fixed-station modes in 2020. This was repeated in 2023 when it was set in 150 scan stations, comprising 44 scans for the general perpendicular geometry mapping of the TCTC and 106 scans for 3rd-level CH details in the corridors and interiors of the six temples.

Finally, to map the 3rd level of CH detail, the object-element geometry level, a close-range measurement by handheld low-cost Lidar (the bas-relief part and corridor part of the TCTC), spherical photogrammetry (the corridor part of the TCTC), and the TLS (detailed façade) were adopted. In this case, spherical photogrammetry has been proven to be

accurate for CH corridor mapping [42,64–67]. To implement this technique, a low-cost Ricoh Theta 360° 12 Megapixel spherical camera and Ipad Pro 2020 Lidar were utilized.

2.4. Data Processing

Photographs collected from each photogrammetry were processed following the standard Structure-from-Motion (SfM) pipeline, which includes feature detection and matching, SfM bundle adjustment, and multi-view stereo (MVS) matching [68,69]. It produces 3D dense point clouds, 3D textured mesh, and orthophotos [23,34,69]. Besides that, raw point clouds from each Lidar scanning were processed using registration, filtering, and georeferencing procedures [35,36,70,71]. This process creates a combined, registered, and georeferenced point cloud. Both of the data processing methods require and include GDCPs and FDCPs in the procedures. For the implementation, Agisoft Metashape v1.8.4, Maptek Point Studio v2022.1, and CloudCompare v2.12.4 (https://www.danielgm.net/cc/ accessed on 28 October 2023) were used.

2.5. Data Integration

To integrate the results from each sensor, we followed a scenario diagram for data fusion in our workflow (Figure 2). It included a detailed combination procedure until the data were completely fused. Hierarchical integration from the least detailed CH-level data fusion to the most detailed CH-level data fusion was introduced. Firstly, the planar topography data from both aerial Lidar and photogrammetry were integrated seamlessly by GDCPs. Secondly, the same GDCPs were also used as their scanning station for the direct georeferencing process of the perpendicular geometry data from the TLS. This allowed the point cloud data to be well-positioned to the same reference as the planar topographic data. Other photogrammetry data (CR-UAVP mode and terrestrial mode), which measure the same target as the TLS, used FDCPs as their reference. These first two steps can be classified as independent georeferencing, as they were georeferenced separately but used common reference points [29]. Because these first two steps may not be perfectly accurate, the so-called 'refinement registration' by the iterative closest point (ICP) algorithm, which benefits from overlapping surfaces [72], was performed in the third step. In this regard, well-scaled TLS data were used as the master data and photogrammetry data as its slave data to be registered. Finally, the object-element geometry data from photogrammetry and low-cost handheld Lidar were also registered to the main combined model.

2.6. Evaluation and Assessment

Once the combined model was obtained, the assessment was carried out. The objective was to ensure that the final model was complete, precise, and accurate. This was performed by several methods: visual inspection, root mean square (RMS) error, cloud-to-cloud (C2C) distance analysis, and multiscale model-to-model cloud comparison (M3C2) [73]. Visual inspection was used to assess the completeness of the combined model qualitatively according to the real-world condition, while RMS was used to assess the geometric accuracy of the combined model compared to the real-world dimensions. C2C analyzes the closest Euclidean distance between two sets of compared point clouds [29], while M3C2 measures the Euclidean distance along the local normal vector by using the local average of neighborhood points assumptions [74]. Generally, C2C has been extensively used to compare the photogrammetric point clouds to the reference clouds that are usually from a TLS, as found in [29,75–78]. This procedure was adopted for this research. In our case, C2C and M3C2 were used to evaluate the mean distance of two sets of point clouds. Both C2C and M3C2 were used to evaluate the consistency of the results.

2.7. Visualization

The combined model is primarily presented as façade point clouds, orthophotos, and a 3D textured mesh, with potential future development of a reality-based 3D solid model. The first two models are the main output of SfM and point cloud processing, while the last two models are the result of post-processing activity involving both the Poisson Reconstruction algorithm [79] in CloudCompare v2.12.4 software and the Scan-to-BIM pipeline [28,80,81] in Revit 2024 software. These reality-based model outputs can further be capitalized to create an HBIM model for further CH management and analysis.

2.8. Search for Architectural Rules and Patterns

To validate and demonstrate the usefulness of the combined model for CH analysis, the 3D point cloud model was analyzed. This examination aimed to prove that architectural design attributes previously identified as construction rules [7,8,12] remain relevant and applicable to contemporary CH conditions. We intended to find the existence of the intentional (1) planimetric and vertical design, namely, the Cartesian–cruciform and triangle-shaped silhouette (Mahameru concept), (2) the directional axis design, (3) the symmetricality concept, (4) the scale and proportion concept, (5) the harmony and repetition concept, (6) the tripartite concept, and (7) the hierarchical concept of the TCTC using several types of measurements to the combined model. The horizontal, vertical, and/or slant distances were repeatedly measured for several parts of the combined model. Several of the measured variables of every design attribute were then tabulated and analyzed to find the true existence of design attributes.

3. Results

3.1. The Geometric Quality of Each Sensor

The quality assessments of the results in terms of the root mean squared error (RMSE) of the X-Y coordinate and the dimension are summarized in Figure 5.

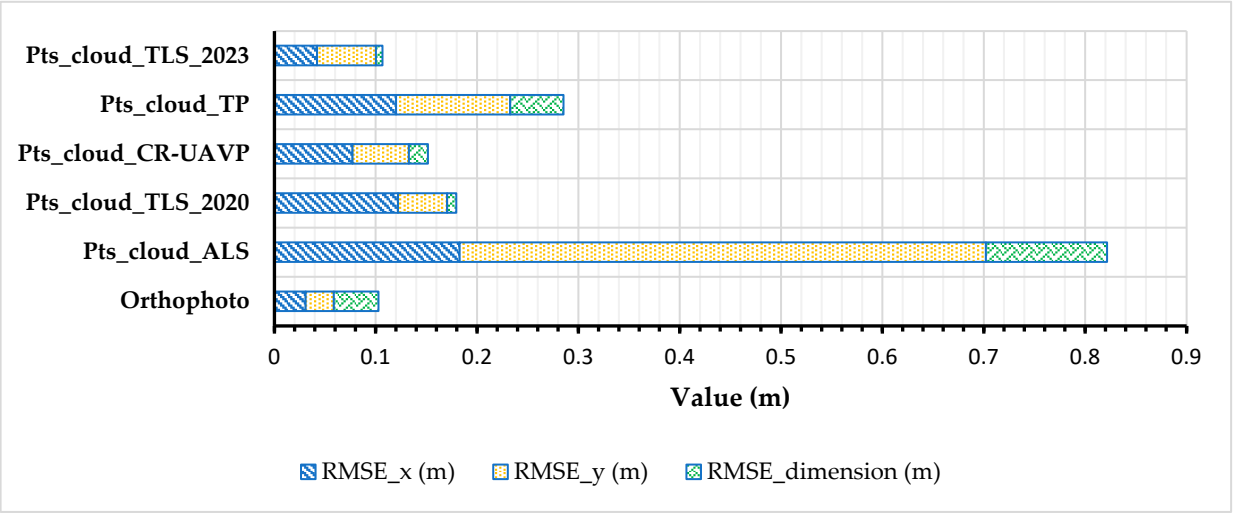

Figure 5. Summary of the quality assessment of each sensor processing result.

3.1.1. Individual Assessment of Photogrammetry Data

The nadiral photogrammetry products, i.e., orthophotos (see Figure 6), were generated by following the SfM pipeline. The total error of bundle adjustment to 211 nadiral photographs is 4.9 cm, which produces about 8 mm GSD. This initial processing uses a combination of direct georeferencing using embedded RTK GNSS coordinates (see Section 2.3) and indirect georeferencing using three GCPs and two ICPs from GDCPs. This limited GCP

number is caused by data availability issues, ground pillar post-marking visibility issues, pillar coverability issues, and pillar condition quality issues at that observation time. Here, the GCP and ICP referred to the GDCP version 2020. Now, these GDCP coordinates have been updated to the 2022 version. Thus, the orthophoto was transformed to this reference by performing a polynomial transformation using seven GDCP common points (three at the main zone and four at the buffer zone) at different epochs. After the transformation, the comparison to 39 absolute coordinates from RTK GNSS observations and 28 reference dimensions obtains RMS errors of 3.1 cm, 2.7 cm, and 4.4 cm in the X component, Y component, and dimension, respectively (see Figure 5). Generally, the internal quality depicted by the total error of bundle adjustments and resulting GSD can be categorized as the third of the 1:1000 map scale according to Indonesian national standards. In addition, the external quality depicted by RMS error still falls within tolerance. Other than orthophotos, there are side products such as point clouds and 3D textured meshes.

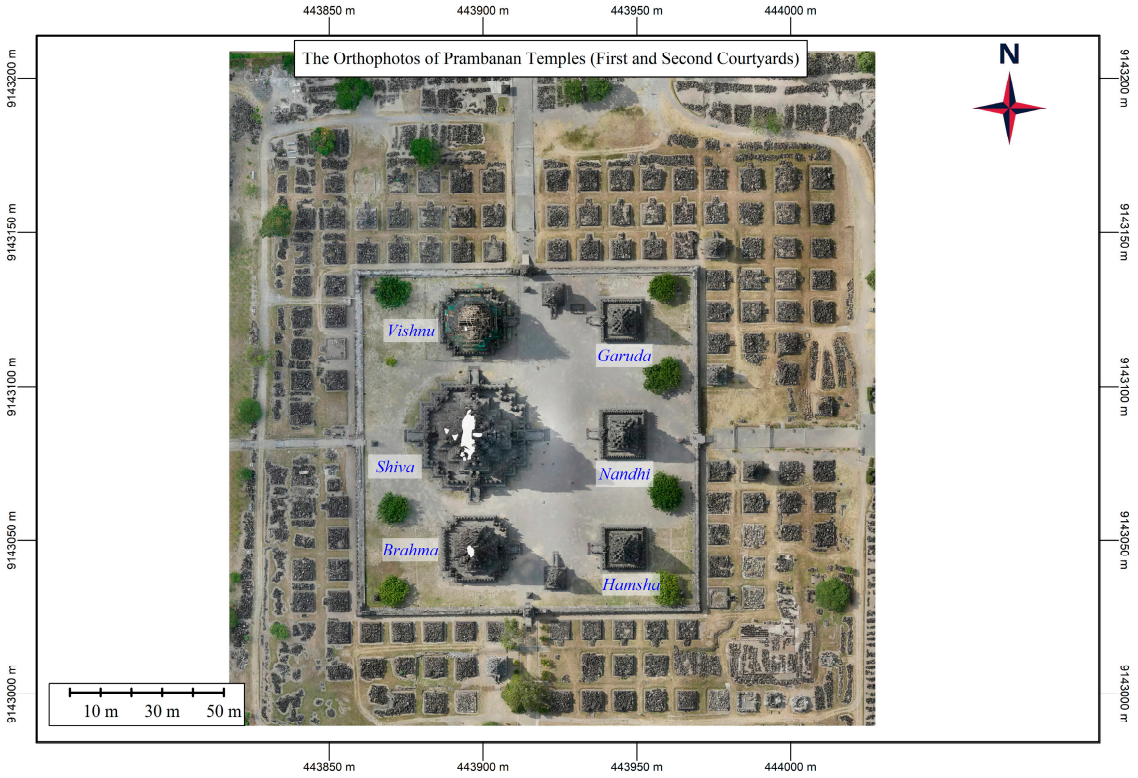

Figure 6. Orthophoto result of the sites that cover the first and second courtyards.

3.1.2. Individual Assessment of TLS Data

The second product, i.e., registered and georeferenced 3D point clouds (see Figure 7), is from the TLS observation. There are 79 scans in the 2020 epoch and 150 scans in the 2023 epoch, with 6 mm/10 m and 12.5 mm/10 m density captured at a 1 m and 3 to 5 m distance surrounding the temples to be processed. Six of these scan data series were captured under direct georeferencing mode (fixed-stationing mode), where the TLS was set at an occupation station (at a GDCP) and then oriented to the backsight station (other visible GDCP) before the scanning process. This allowed us to obtain directly georeferenced scans. Then, these were used as a reference to register the rest of the free scans using the ICP algorithm. This was then followed by a filtering process. Finally, registration RMS errors for both sets of data were obtained, which depict their internal quality.

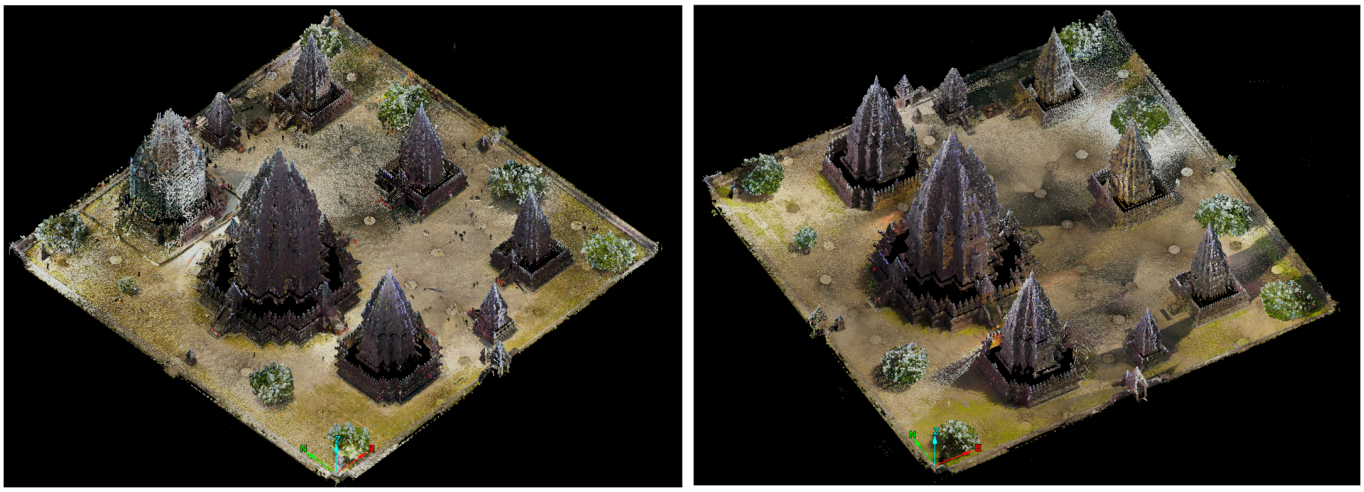

(**a**) (**b**)

Figure 7. Registered and georeferenced 3D point clouds from (**a**) TLS 2020 and (**b**) TLS 2023.

The registration RMSE of the 2020 data ranges from 9 mm to 47 mm (outdoor area) and 6 mm to 35 mm (indoor area), while the registration of the 2023 data generates RMS errors ranging from 10 mm to 29 mm (outdoor area) and 3 mm to 29 mm (indoor area). Then, the selected 35 samples of dimensions and 48 samples of coordinates of processed point clouds were compared to the corresponding ground truths to assess the external quality represented by the RMS error. The initial mean of X and Y coordinate differences are 3 mm to 4.6 mm (TLS 2023) and 3.7 mm to 11.1 mm (TLS 2020), while the mean dimension differences are 4 mm and 7 mm. The RMS error of the X component (RMSEx), Y component (RMSEy), and dimension (RMSEdim) of the 2023 data are 42.1 mm, 58.2 mm, and 6.51 mm, respectively, while the 2020 data have relatively higher RMSEx (122 mm), lower RMSEy (48.5 mm), and higher RMSEdim (8.98 mm) compared to the 2023 data (see Figure 6). This indicates that the TLS data (2023) have the most accurate position and dimension among the available point cloud data (orthophotos are excluded). Hence, they were used as reference data in the shape closeness comparison (see Section 3.2).

3.1.3. Individual Assessment of Aerial Lidar Data

The third product is UAV Lidar point cloud data (see Figure 8). The data are sparse in density (16 cm point spacing or 667 points/square meter), referred to as GDCP 2020, and mostly target the topography or landscape. These data were aligned to the GDCP 2022 reference by 3D rigid transformation (4 × 4 matrix—translation and rotation) or match bounding box centers (MBBCs) [82] using 11 post-mark common tie points corresponding to the TLS data (2023), and a transformation RMS error of 32 cm or 2 sigma (resolution) was obtained. After comparing 48 coordinate and 33 dimension samples, the results show mean coordinate differences of 16.1 cm to 50.8 cm and mean dimension differences of 9.5 cm, resulting in RMSEx, RMSEy, and RMSEdim of 18.2 cm, 51.9 cm, and 11.9 cm, respectively (see Figure 5). These large RMSE values (in Figure 5) are probably caused by the low density of the point clouds, which could create inaccuracies and increase uncertainties in sample point picking. It should be noted that this nadiral UAV Lidar focuses on topography scanning for a relatively large area rather than façade scanning; therefore, it contains minimum or incomplete façade data where all the samples originally came from. That is why it is less accurate or has a large RMSE (see Figure 5). It is only suitable for fast and large topography mapping purposes.

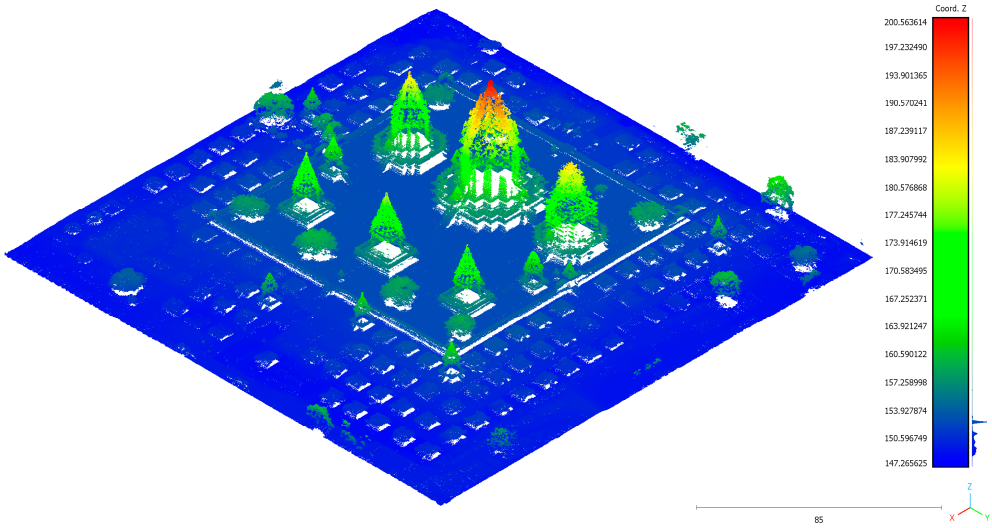

Figure 8. Point cloud model from aerial UAV Lidar.

3.1.4. Individual Assessment of Close-Range UAV and Terrestrial Photogrammetry Data

For close-range UAV and terrestrial photogrammetry products, i.e., dense point clouds (see Figure 9) that focused on the façade shape of each of the six main temples, the internal and external quality exhibit various results. Internal quality refers to the RMS of all tie points' reprojection error (or Σ image error) and the total error value from the bundle adjustment process. See Table 3 for details of the six main temple bundle adjustment processing parameters and results.

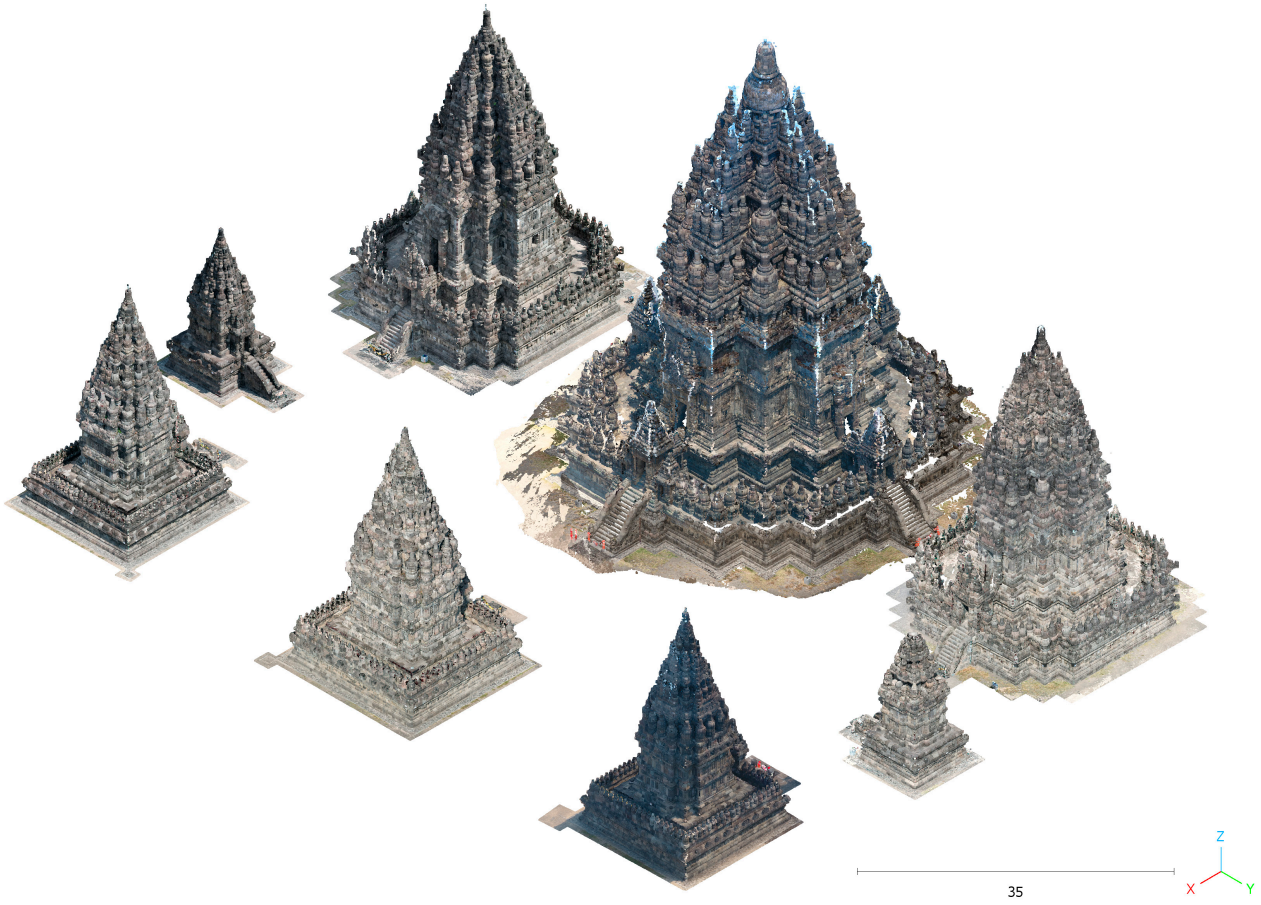

Figure 9. Dense point cloud model from CR-UAVP integrated with terrestrial photogrammetry.

Table 3. Selected processing parameters and results of the SfM bundle adjustment of the six main temples.

No	Temple	Σ Images	Σ FDCP	Σ Coded Target	Σ Image Error (Pixel)	Total Error (cm)	Σ Tie Points	Tie Points Limit per Photo	Σ IOP Included	Camera ID
1	Shiva	595	4	n/a	0.601	4.19	458,875	4000	8	FC330
2	Garuda	229	3	n/a	0.758	0.817	93,874	4000	8	FC330
3	Vishnu	542	3	10	0.854	4.6	92,113	4000	9	Test_Pro
4	Nandhi	277	3	13	1.52	2.289	23,882	1000	7	Test_Pro
5	Brahma	475	3	6	1.15	3.97	35,754	1000	8	Test_Pro
6	Hamsha	295	3	19	1.14	3.18	20,581	1000	8	Test_Pro

Table 3 shows that the total error is mostly within 2 cm–4.6 cm, except for the Garuda result (0.8 cm), and the Σ image error is close to 1 pixel, except for the Nandhi result (1.52 pixels). Furthermore, the processing report (Table 3) reveals important findings. By using the same camera ID and acquisition technique while significantly increasing the tie point limit per image, a notable decrease in the total reprojection error due to the higher total number of tie points was observed. Additionally, maintaining the same camera ID and flight mode but incorporating more interior orientation parameters (IOPs) into the reprojection process led to an acceptable reprojection error. These are the most probable reasons behind the non-subpixel image error obtained. Note that all of these results are the combination of close-range UAV and terrestrial photogrammetry, except for the Garuda, Nandhi, and Hamsha Temples.

Moreover, the external quality of the dimension aspect (RMSE dimension) and the horizontal position (X, Y) aspect (RMSE x and RMSE y) are 1.88 cm, 7.71 cm, and 5.55 cm, respectively, when compared to a sample of 68 dimensions and 33 coordinates from RTK GNSS (see Figure 5). It is slightly higher than the RMS error of the TLS 2023 data; therefore, this result seems promising for multi-source integration purposes.

3.1.5. Summary of the Quality Assessment

Based on the above-mentioned assessment, the assessed datasets can be distinguished into two types: planar topography and perpendicular geometry. The first type of dataset (landscape topography) includes nadiral UAV Lidar and nadiral UAV photogrammetry products. These two datasets show different accuracies. The nadiral UAV photogrammetry product, i.e., the orthophoto, provides significantly better positional and dimensional accuracy compared to UAV Lidar point clouds (and the rest of the point cloud dataset) (see Figure 5). This is expected since both data have different natures (ortho-imagery vs. sparse point set). The orthophoto enables the easy selection of sample coordinate points and dimension measurements, which is not possible with the sparse point set.

Moreover, the second type of dataset (perpendicular geometry) includes the TLS, CR-UAVP, and terrestrial photogrammetry (TP) datasets. Their main product is a dense point cloud of six main temples. After the assessment, it was shown that the TLS 2023 data have the lowest internal and external RMS error range, followed by CR-UAVP, TLS 2020, and TP (see Figure 5). In this study, the integrated photogrammetry's (CR-UAVP plus TP) dense point cloud provides a slightly higher RMS error range. However, in a more robust setup, the result is expected to be equal to or even outperform the TLS accuracy. In addition to the accuracy aspect, it is also important to inspect the completeness aspect. In this study, the TLS 2023 dataset provides more complete coverage than any of the integrated photogrammetry point clouds. It almost covers all parts of the temples (except the upper part) and covers all of the main courtyard topography (see Figure 7). Due to its accuracy and completeness, the TLS 2023 dataset was selected as the reference dataset to be compared to the other dense point cloud dataset.

3.2. Combined 3D Point Cloud Model from Multiple Sensors

After individual data processing and quality assessment, the data integration scenario mentioned in Section 2.5 was performed. It is important to note that only the point cloud datasets were combined. The assessed orthophotos in Figure 6 were not. The sample result of the point cloud combination of the Brahma Temple is presented in Figure 10. The other temples are similar to this example.

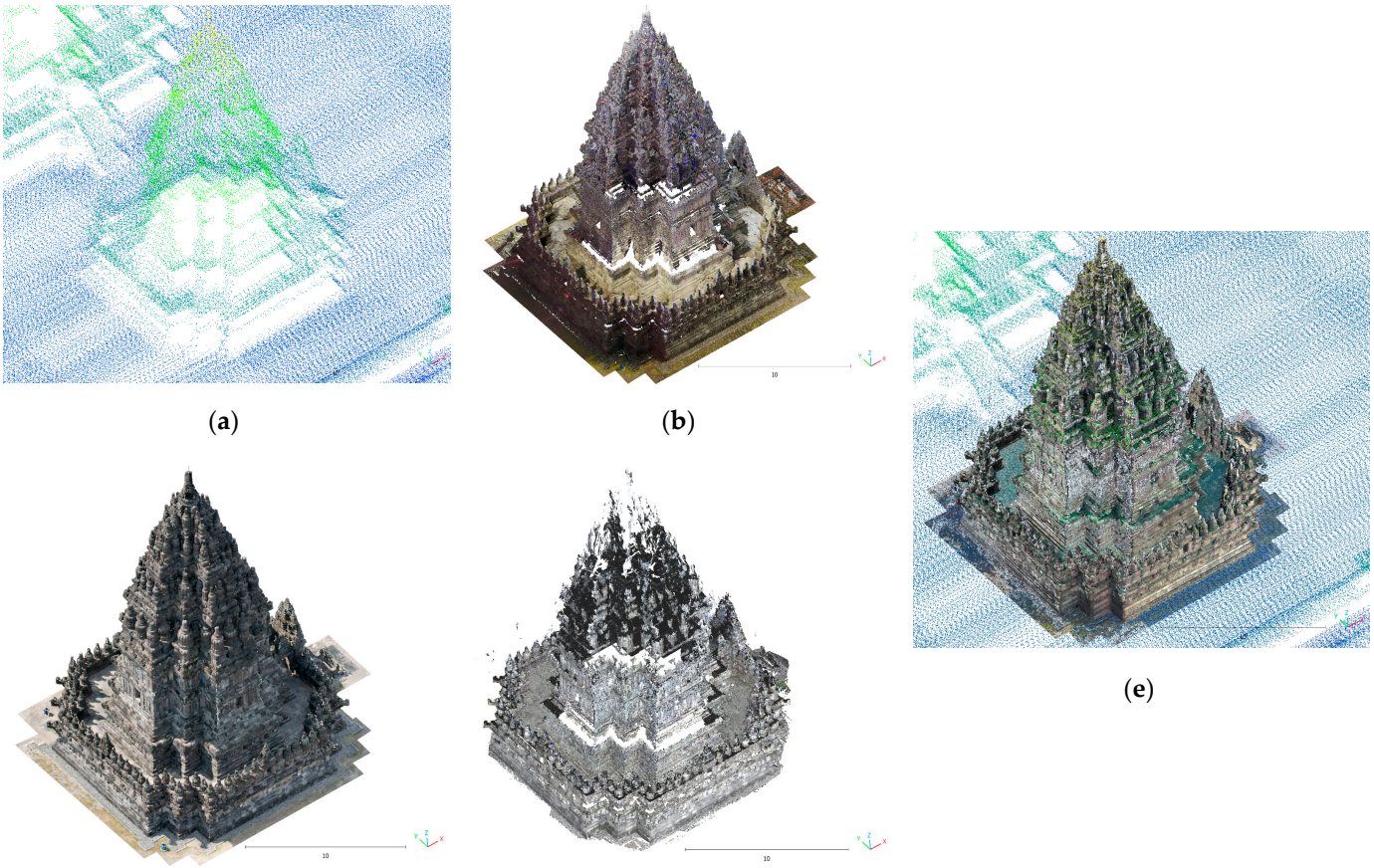

Figure 10. Point cloud results from multiple sensors and their combinations (the example of the Brahma Temple). (**a**) Nadiral UAV Lidar; (**b**) TLS; (**c**) CR-UAV photogrammetry; (**d**) terrestrial photogrammetry; (**e**) combination of each sensor point clouds. The true color and texture of the temple are presented by (**b**–**d**), while (**a**) only displays the scalar color scale based on the Z coordinate.

3.3. Adjacency or Closeness Between Data (M3C2 and C2C) and Adjacency to Check Data

After combining the 3D final point cloud models from the multiple sources above, the model similarity and closeness between the point cloud datasets that constitute the final model were analyzed by C2C and M3C2 distance analysis. It was only subject to the overlapped dataset, such as (1) between two epochs of the TLS data and (2) between the TLS data and the integration of the CR-UAVP and the terrestrial frame photogrammetry data (see Figure 11). This comparison starts from the assumption that if the datasets are similar in shape and intersect well with each other, the gap between the datasets is minimal. In this regard, the reference data were TLS 2023 data as they had the highest accuracy compared to the other point cloud datasets.

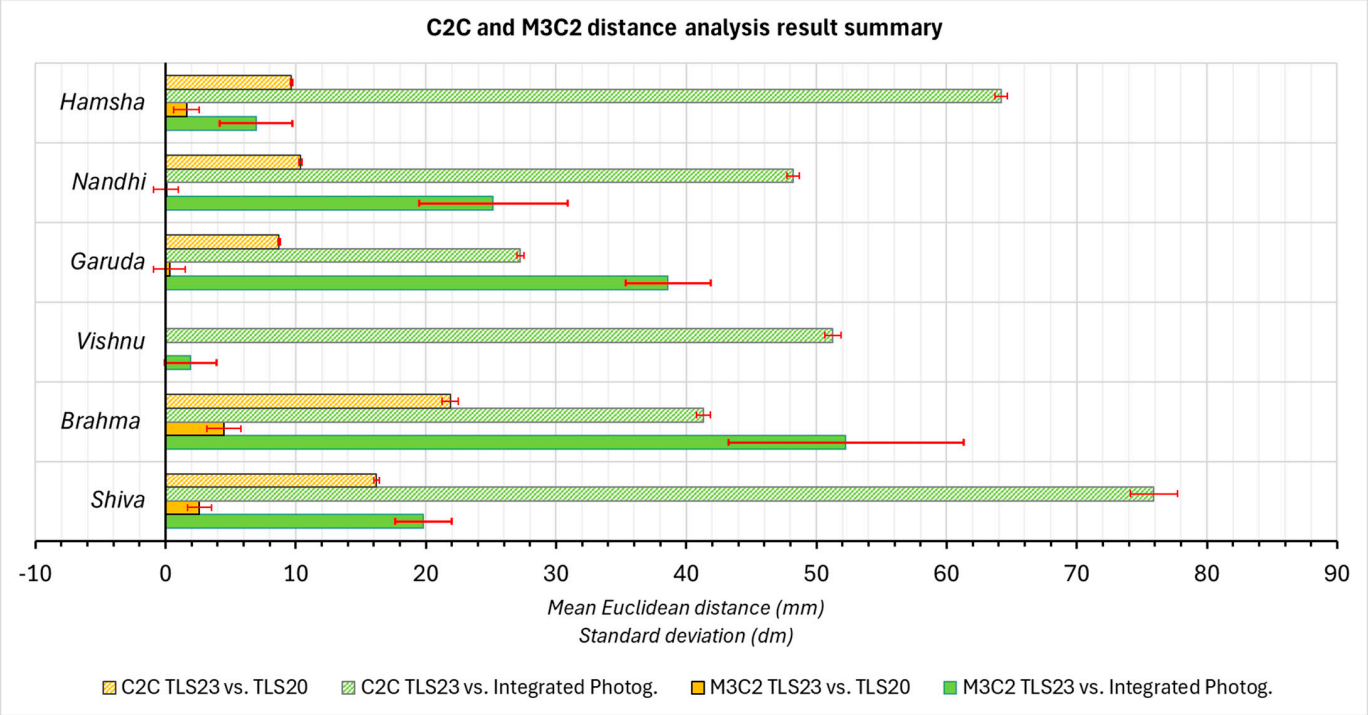

Figure 11. C2C and M3C2 Euclidean distance analysis results of the six main temples of interest.

The first comparison between two different epochs of the TLS data (2020 vs. 2023) shows that the mean Euclidean distance between two datasets in C2C analysis ranges from 8 mm to 21.8 mm over the entire overlapped regions (see Figure 11). Note that Vishnu was undergoing rehabilitation at the time the TLS 2020 data were collected, which precludes comparison. Every temple dataset has different C2C results. The mean Euclidean distances among data pairs for Garuda, Hamsha, Nandhi, Shiva, and Brahma are 8 mm, 9.6 mm, 10 mm, 16.2 mm, and 21.8 mm, respectively (see Figure 11—orange-shaded bar). The distance value sample distribution is minimum, as demonstrated by the low value range of the standard deviation. On the other hand, the M3C2 results of these common datasets of interest show significantly low mean Euclidean distance values of 0.29 mm (Garuda), 1.6 mm (Hamsha), 0.044 m (Nandhi), 2.61 mm (Shiva), and 4.47 mm (Brahma). The variation in the distance values is slightly higher than C2C. These lower mean distance values might benefit from local average assumptions within the M3C2 algorithm. The comparison of these two algorithms demonstrates a consistent millimeter range of relative mean Euclidean distance values between data pairs. Therefore, it can be concluded that the dataset of interest has a similar shape or a smaller gap compared to the master dataset (TLS 2023).

The next comparison is between the TLS data (2023) as the master data and the CR-UAVP plus terrestrial photogrammetry data as the slave data. In this regard, every temple of the six main temples located in the main courtyard was examined using M3C2 and C2C distance analysis. As shown in Figure 11, the mean Euclidean distance that incorporates the local average assumption in the M3C2 analysis of every temple gives values of 1.9 mm for the Wishnu Temple, 8.95 mm for the Hamsha Temple, 19 mm for the Shiva Temple, 25 mm for the Nandhi Temple, 38 mm for the Garuda Temple, and 52 mm for the Brahma Temple. The distance value distribution of the Vishnu dataset is close and clustered to a zero value, implying a smaller gap across the two compared datasets. This is contrary to the distance value distribution of the Brahma dataset, which varies more in values and is far off from zero. On the other hand, the C2C analysis indicates a higher centimeter

range of the mean distance values (27 mm to 75 mm) with a less varied value distribution (small standard deviation range). The biggest value of the C2C mean distance is obtained from the Shiva dataset (see Figure 11). This is due to the imperfect reconstruction of the temple corridor (see Figure 12). The UAV is unable to closely capture and take sufficient overlapping images in this area due to safety reasons. Despite this limitation, all mean Euclidean distances fall within the centimeter range (0.19 to 7.5 cm) and are relatively small compared to the entire structure and dataset. This suggests that the data are fairly similar to the reference data.

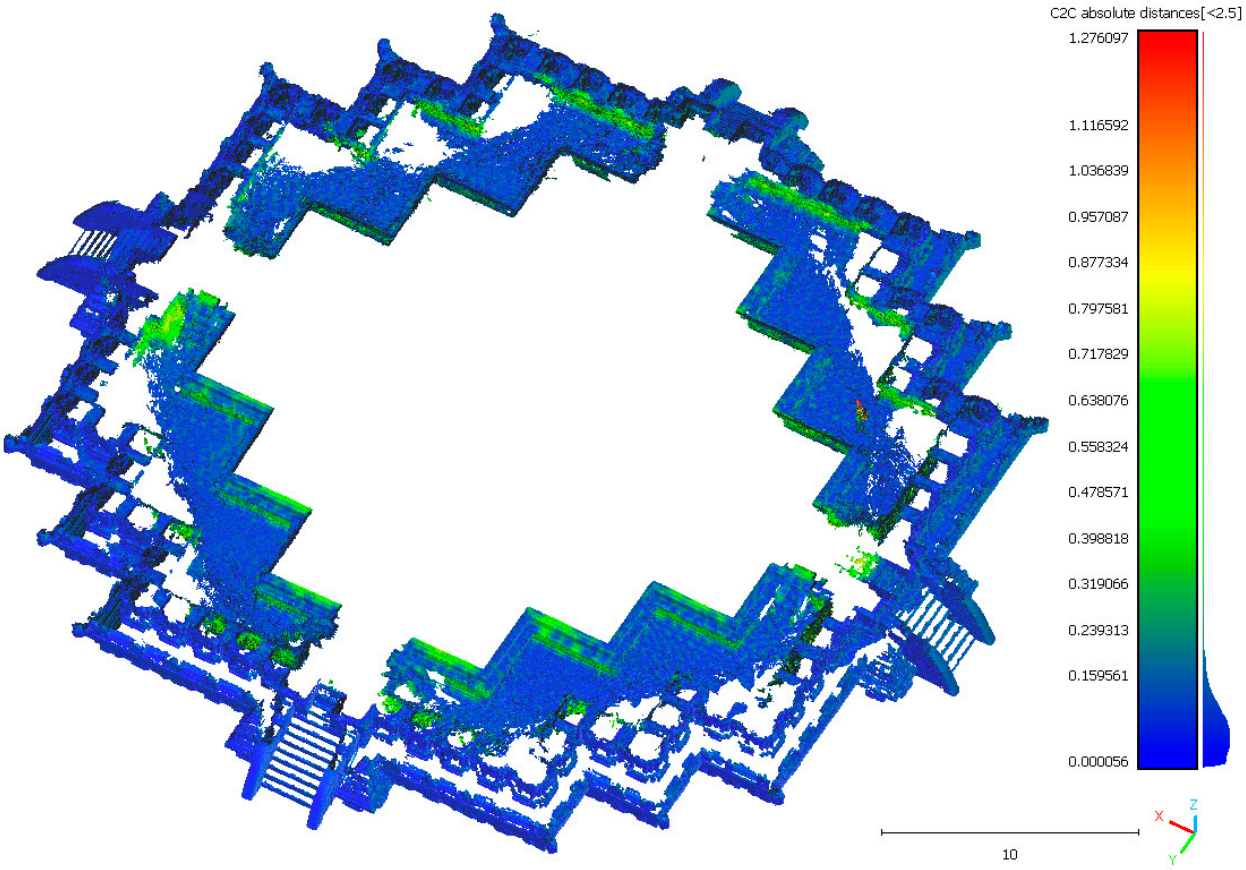

Figure 12. C2C results of the corridor part of the Shiva Temple.

Referring to all comparisons, there are major similarities between the datasets. On the other hand, the reference data (TLS 2023) have a millimeter level of positional and dimension accuracy. This proves that the model will combine effectively when loaded together with an accurate absolute position. This suggests that the proposed data combination flow is a proper procedure to combine multi-resolution models from multiple sensors.

3.4. The Proof of the Existence of Several Architectural Design Attributes of the Temples

The final combined model was validated, and it was used to examine architectural rules and patterns within the temples. As hypothesized by [7], there were exact design patterns, i.e., planimetric proportion, namely, (1) rectangular-based and (2) Cartesian–cruciform. The search for these patterns involved several measurements of the 3D point cloud model, as shown in Figure 13.

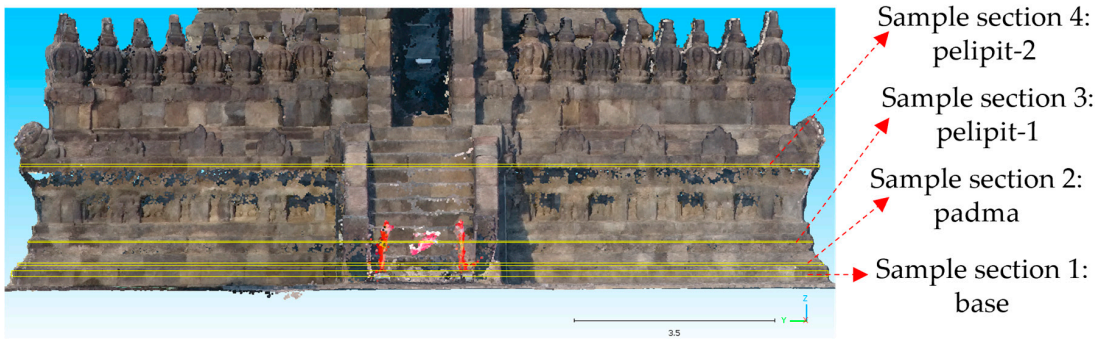

Figure 13. Four sample measurements captured on the base part (Bhurloka) of a single temple.

The series of repetitive measurements of planimetric dimensions to the 3D point cloud model (see Figure 13) of the six main temples demonstrates that there is an exact proportion of 1:1 width (w) and length (l) in both the Garuda and Hamsha Temples' planimetric geometry and a 1:1.1 width and length proportion in the Nandhi Temple (Figure 14). The planimetric design of these three temples is considered rectangular-based. Besides that, the other three bigger temples tend to have more complex Cartesian–cruciform designs. The parameters w1, wp1, wu1, and wt1 represent every east–west (E-W) orientation side part, and w2, wp2, wu2, and wt2 represent every north–south (N-S) orientation side part (see Figure 15). The series of planimetric dimension measurements on the base part (Bhurloka) of the 3D point cloud model of the temple shows that there is a similar proportion of the Wishnu and Brahma Temples, but these two temples have different proportions to the Shiva Temple (see Figure 16). In this regard, both the Brahma and Vishnu Temples have an average proportion of w1:wp1:wu1:wt1 = ±11.1:1:7.1:1, and w2:wp2:wu2:wt2 indicates the same result (see Figure 16). These Bhurloka parts of the temple are then considered as symmetrical congruence geometry. The Shiva Temple, on the other hand, has its own average proportion of w1:wp1:wu1:wt1 = w2:wp2:wu2:wt2 = ±10.4:1:6.4:1 (see Figure 16). The 3D points cloud model for the body (Bhuvarloka) and roof (Svarloka) were also measured to ensure that the planimetric proportion at the base is precisely maintained up to the uppermost part (see Figures 17–20). However, due to the imperfect shape (deformed shape and lines, as well as curvy and spalled corners), the proportion of these two regions cannot be precisely maintained.

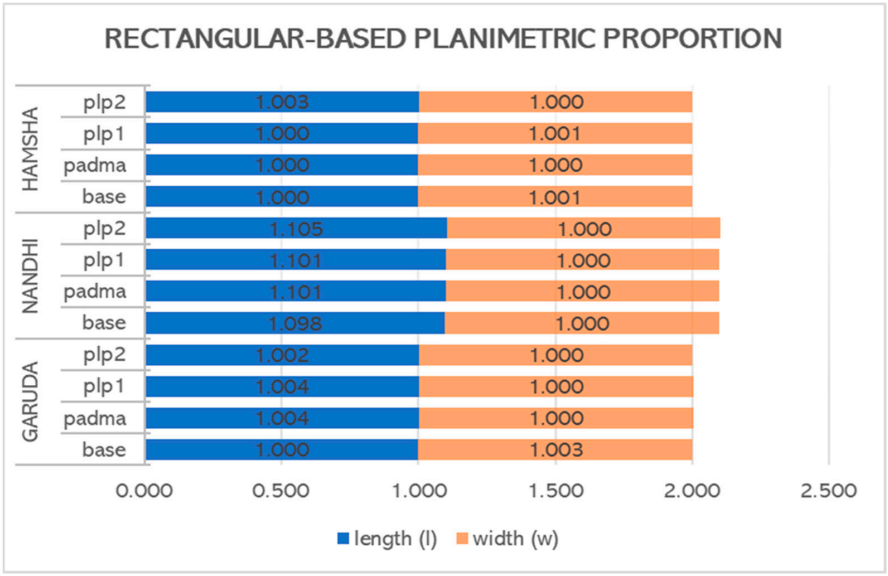

Figure 14. Rectangular-based planimetric proportions of the Garuda, Nandhi, and Hamsha Temples.

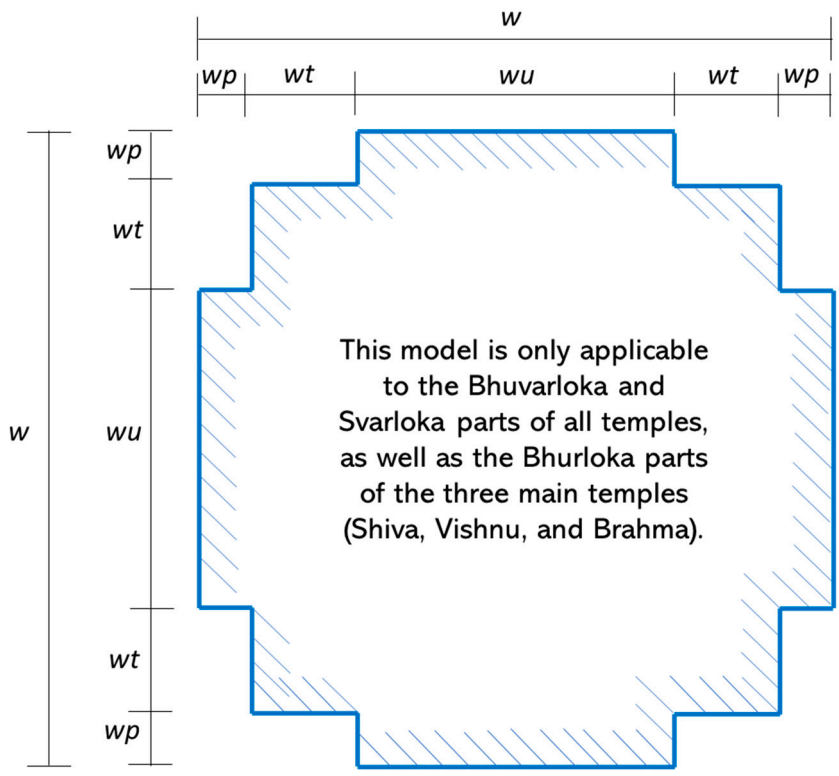

Figure 15. The parameter of the Cartesian–cruciform-based planimetric proportion.

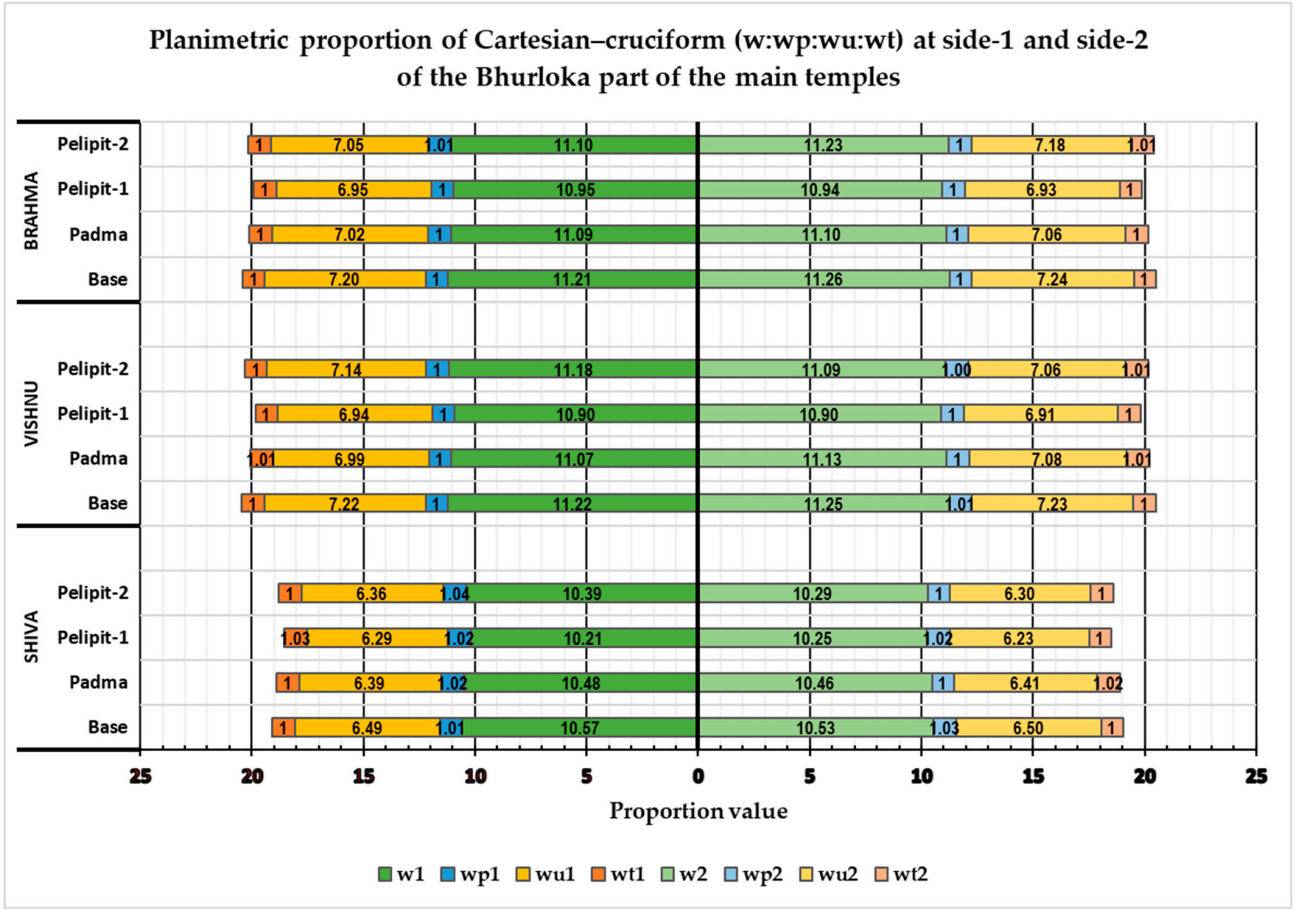

Figure 16. Cartesian–cruciform planimetric proportion of the Shiva, Vishnu, and Brahma Temples (Bhurloka part).

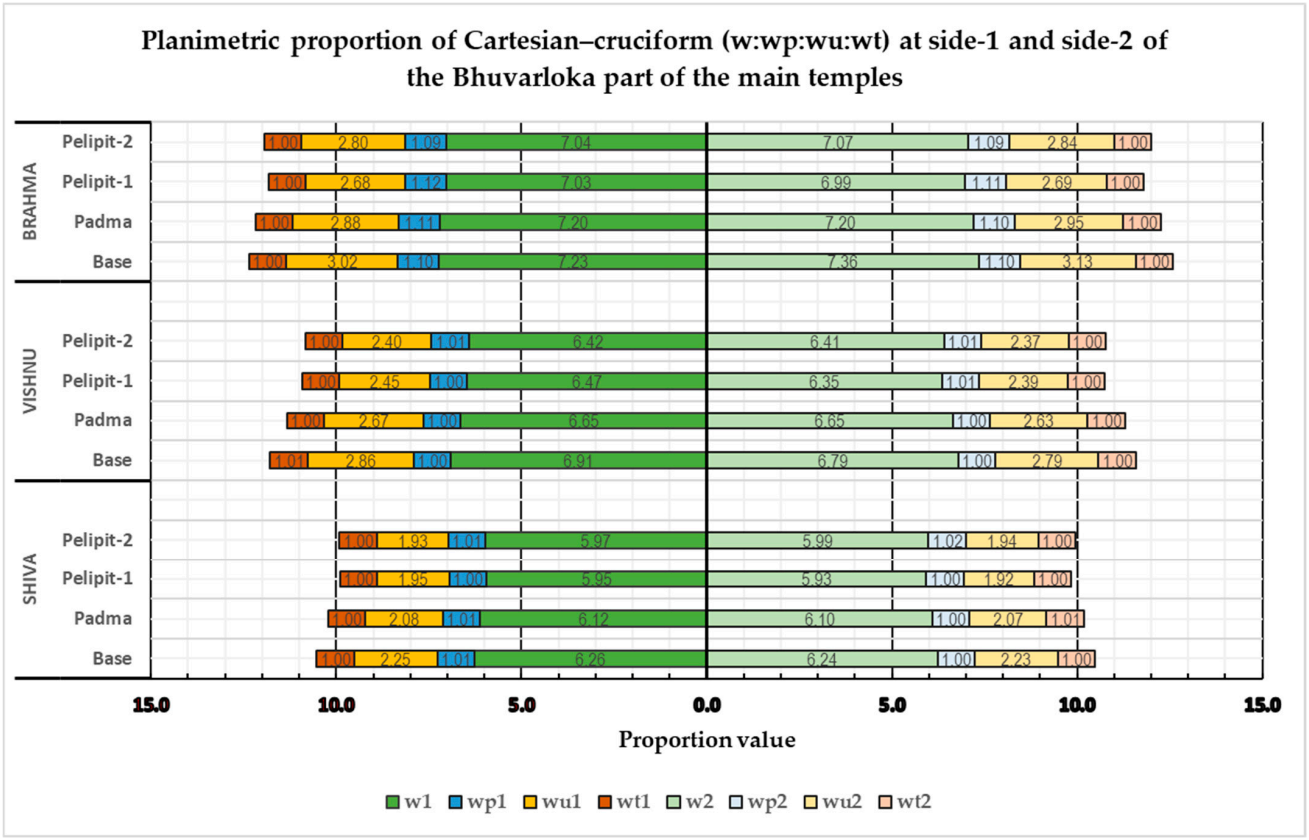

Figure 17. Cartesian–cruciform planimetric proportion of the Shiva, Vishnu, and Brahma Temples (Bhuvarloka part).

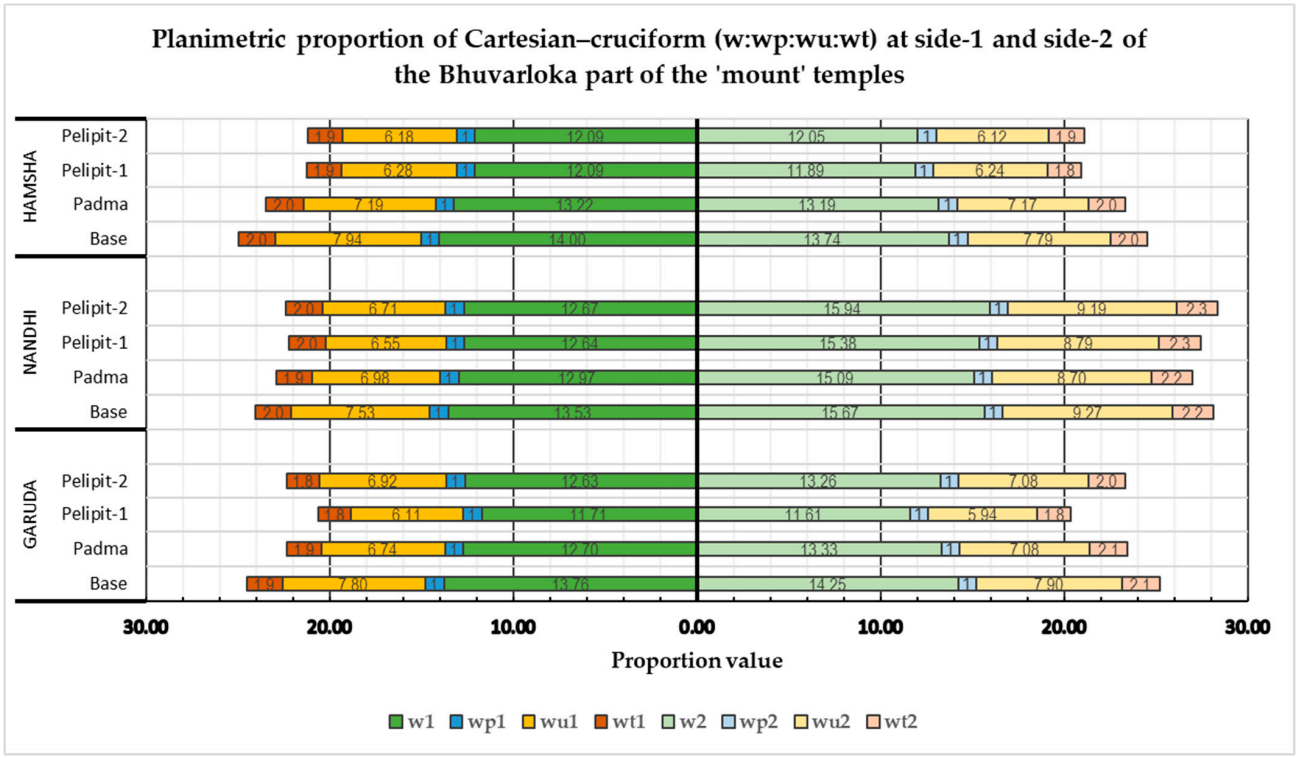

Figure 18. Cartesian–cruciform planimetric proportion of the Garuda, Nandhi, and Hamsha Temples (Bhuvarloka part).

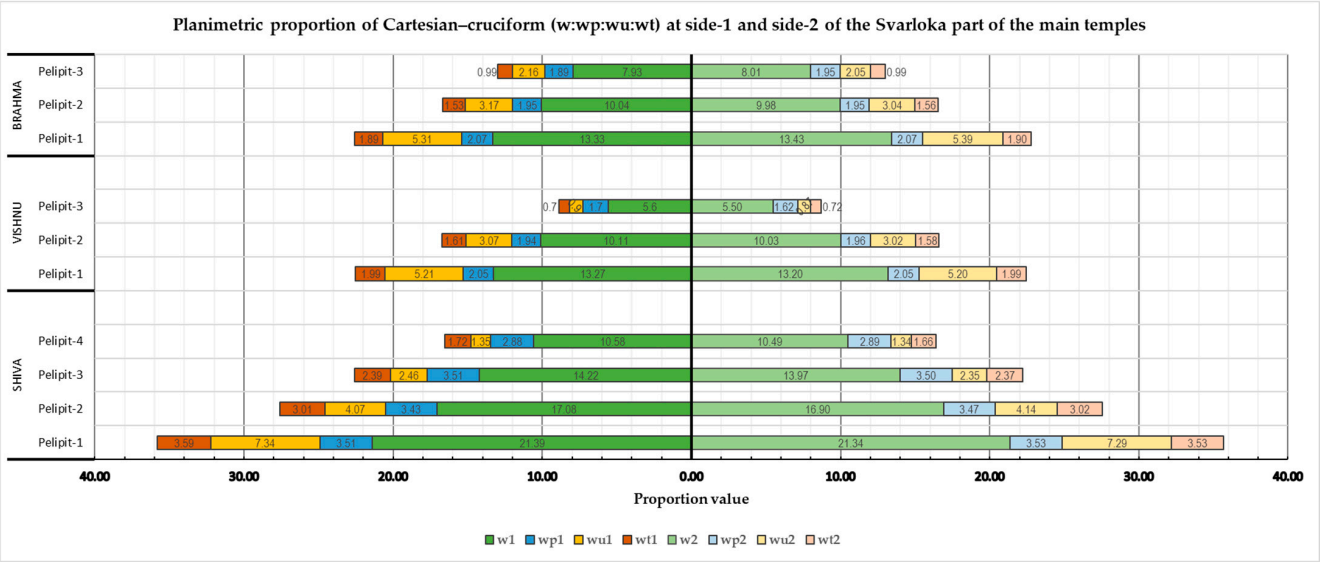

Figure 19. Cartesian–cruciform planimetric proportion of the Shiva, Vishnu, and Brahma Temples (Svarloka part).

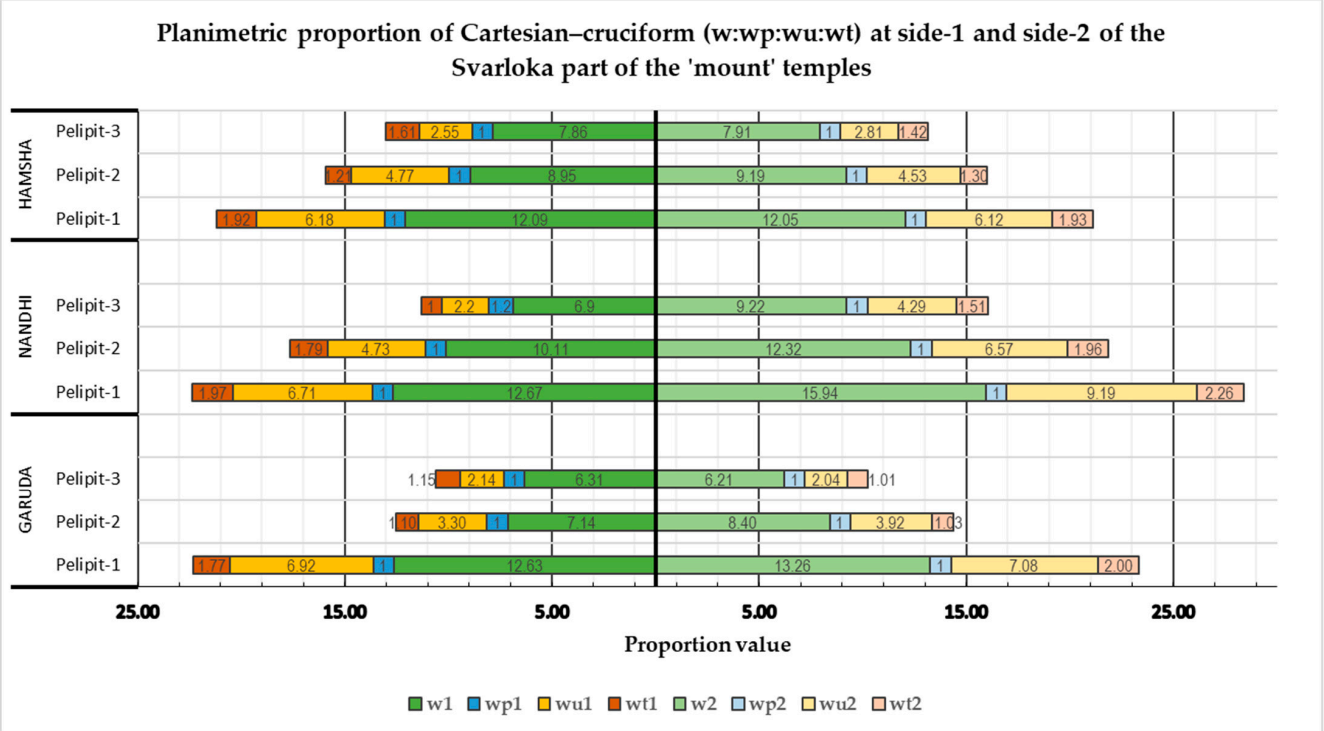

Figure 20. Cartesian–cruciform planimetric proportion of the Garuda, Nandhi, and Hamsha Temples (Svarloka part).

These experiments affirm various findings: (i) the Garuda and Hamsha Temples exhibit identical rectangular-based planimetric proportions of 1:1 (width–length), whereas the Nandhi Temple, the largest in the central 'platform' temple series, displays a proportion of 1:1.1; (ii) the Brahma and Vishnu Temples share a similar Cartesian–cruciform proportion, though the Shiva Temple, the largest in the Mahadeva Temple row, differs slightly; and (iii) these proportions are not exactly maintained to the topmost part.

To determine why the planimetric proportion was not properly maintained to the topmost part, the temple's restoration history was traced, and it was found that a smaller

temple underwent extensive restoration (or even complete dismantling) after its collapse, involving the addition of a concrete frame skeleton, mortar resin between stones, and the installation of new stones [5]. This indicates that the restoration process on the body and roof may not fully preserve or maintain the original pattern design. In this regard, the researcher in [5] reveals that only the Shiva Temple maintains its originality during the restoration process, while the others are unlikely to. Upon its first discovery, it measured only 10 m in height; hence, the current additional height of 37 m is due to the restoration work undertaken from 1937 to 1952. This was also confirmed by a 2009 technical report from the Indonesian archaeological office [83]. Our findings align closely with this fact.

4. Discussion

4.1. How Does the Architectural Pattern Design (APD) Influence the Data Acquisition and Processing?

The TCTC Prambanan site was mapped based on hierarchical detail levels and various distinct sensors (see Figures 9–11). The scale-level definition inferred from APD was used to select an appropriate measurement sensor (Table 2) and its associated processing method (Figure 2). In this case, APD gives hidden suggestions that the site comprises a conception/abstraction/philosophy/dimension series, i.e., its landscape, its physical monument, and its deeply inherent narrative value installed at bas-relief and decorative ornaments. It demonstrates the intelligence of local ancient people in designing such a complex monument with deep phylogenetic aspects [9]. The authors interpret this series of conceptions as guidance in handling the complexity of the monument, i.e., by establishing three different detail levels (Table 2). This establishment gives two advantages: (a) the minimum detail required at each scale level can be defined and (b) sensors can be deployed easily according to the detail level, which leads to unbiased sensor selection. Hierarchical measurements using multiple sensors are then performed by following this establishment, starting from a less detailed scale level (distant sensor location) to a more detailed scale level (closest sensor location). This provides a structured approach to CH documentation. Organizing multiple sensors for the complex monument measurement is challenging. However, by applying this approach, easier, sensible, and structured procedures can be obtained.

When it comes to data processing, data from different sources are processed individually before being combined. In this regard, the GDCPs, as a main ground control pillar network, are distributed to all courtyard zones and take a central role in tying up lower detail level (ground-related) data into single integrated data. Every sensor observes or records its image, enabling independent georeferencing between the data. FDCPs, as a differentiation of GDCPs, are located at temple façades and are used for positional reference for higher detail levels (monument-oriented data). This forms the so-called "hierarchical data processing" by using GDCPs for lower detail levels (landscape and general façade) and FDCPs for higher detail levels (detailed façade and bas-relief). Again, this approach provides a structured method to handle multiple sources of data with multiple detail levels for the TCTC Prambanan case.

The implementation of this approach produces a complete recording of the entire part of the TCTC as the detail level and its corresponding deployed sensor are set for each section of the temple complexes. This, in turn, allows each data point to complement the others (see Section 4.2) and proves the existence of the APD itself (see Section 3.4).

4.2. How Do They Complement Each Other, and Which Parts Remain Unrecorded or Missing?

The orthophoto model from Nadiral UAV photogrammetry (see Figure 6) and the 3D point cloud model of the planar topography from Nadiral UAV Lidar (see Figure 8) provide

complete depictions of the site's core and the buffer zones of the temple complexes. Despite the general completeness, it can be observed that Lidar point clouds are sparse and only record the general geometry of the temple with some blank spots on the perpendicular geometry. On the other hand, the orthophotos are not able to clearly capture the geometry of the upper part of the towering temple since they are not designed to capture tall objects (without extra oblique images); instead, they are designed to capture the topography using nadiral photographs. This limitation was resolved using the CR-UAVP data at the next detail level by using oblique and vertical photographs. As shown in Figure 10, the upper part of the towering temple has now been patched up with point clouds. The scope and coverage of these CR-UAVP data are among the upper part, body part, and some of the bottom part (Table 1 (CR-UAVP)). CR-UAVP data are unable to perfectly capture the bottom part of the towering temple. This limitation was also solved using TLS data and terrestrial frame photogrammetry data (Table 1 (TP)). TLS data capture the bottom part of the towering temple, some part of the body (middle) part, and some of the upper part (Table 1 (TLS)), while terrestrial frame photogrammetry data capture only the bottom part and its installed bas-relief, and terrestrial spherical photogrammetry data capture the corridor part of the temple (Figure 10d). In this regard, photogrammetry not only provides 3D point clouds but also injects color and texture into them, making them more visually realistic [84] and semantically interpreted [78].

This study shows that multiple sensors play an important role in complementing the limitations of each individual sensor, for example, their scope and coverage. When dealing with large and complex sites (e.g., the Prambanan Temple), the multi-sensor data acquisition process is rather challenging [85]. In addition, each sensor has its own scope, coverage, range, mobility, resolution uniqueness, and detail level limitations, as mentioned in [40,85–87]. This study partially addresses these challenges. As discussed in Sections 4.1 and 4.2, the introduction of APD to provide guidance for scale-level development as well as hierarchical multi-sensor data acquisition and processing scenarios is significantly beneficial, particularly when dealing with large and complex heritage sites with clustered objects. This approach allows for a more thorough consideration of architectural aspects during the development of data acquisition scenarios.

4.3. Lesson Learned About Using Multi-Sensor to Document a Concentric Squared Layout of a Temple Cluster

Based on the experiments above, several significant points can be noted. Firstly, in terms of the 3D geometry development, robust Lidar sensors show a consistent result, while the photogrammetry result depends greatly on many factors. In this regard, low-cost Lidar sensors can be excluded because they also show the same nature as photogrammetry. Secondly, for flat façade geometry mapping, both of them tend to have no significant issues in the process, but for the mapping of complex irregular geometry, this is not the case. In this regard, we encountered problems when utilizing multi-mode photogrammetry. Firstly, there is uneven solar radiation during certain observation times, which affects façade brightness (for example, during morning observations, only the east and half of the north and south sides of the façade have enough brightness), resulting in different image brightness values in a single CR-UAVP capture mission. Secondly, there are issues with the homogeneous stone façade texture and color captured in UAV photographs, which disrupt the image alignment process. Thirdly, there are difficulties in providing more dense façade control points in the inaccessible towering façade area (upper part) because of the stone masonry proneness. Therefore, it can be concluded that multi-sensor integration may obtain the best result; however, it may also cause several issues. The issues may stem from variations in the number of outliers, resolution, overlapped area, orientation, and scale. These challenges arise in the cross-sourced point cloud registration process [86]. In this

study, these factors were also encountered. However, by using the proposed workflow, the uncertainty in the registration sequence was reduced.

5. Conclusions

The proposed workflow to handle the documentation of highly decorated, towering, concentric temple clusters (TCTCs) proved to be successful. The architectural design attributes of TCTCs make it intuitive, sensible, structured, and convenient to design the appropriate workflow for many sensor utilizations. This has led to the multiple and hierarchical measurement, processing, and data fusion scenario that must be followed. The implementation of this approach on the Prambanan Temple complex proves that the combined model gives a complete, precise, and accurate result. In the combined model, every sensor with its own limitations can systematically complement each other. The accuracy assessment plays an important role at every scale level, as it ensures the point cloud data are true-scaled and well-positioned before being fused. The final combined model from multi-sensor data fusion is then used as a basis to verify the existence of architectural rules and patterns. It proves that there are clearly intentional design patterns at the most original temple (Shiva) and relatively obscure patterns at other temples due to the rebuilding and restoration process. Therefore, architectural rules and patterns as starting points for heritage documentation consideration as well as for endpoint proof are potentially useful for broader adoption.

Author Contributions: Conceptualization, A.S.P.; data curation, A.S.P.; funding acquisition, A.S.P. and R.M.; investigation, A.S.P. and E.N.A.; methodology, A.S.P.; resources, R.M.; supervision, I.G., I.M. and I.I.; validation, A.S.P. and E.N.A.; visualization, A.S.P.; writing—original draft, A.S.P.; writing—review and editing, A.S.P., I.G., I.M. and I.I. All authors have read and agreed to the published version of this manuscript.

Funding: This research was funded by the Centre for Higher Education Fund (Balai Pembiayaan Pendidikan Tinggi) under the Ministry of Education, Culture, Research, and Technology of the Republic of Indonesia and the Indonesian Endowment Fund for Education (Lembaga Pengelola Dana Pendidikan (LPDP)) through a postgraduate scholarship program, Beasiswa Pendidikan Indonesia (BPI) [ID: 202101120837].

Data Availability Statement: Data are available upon request.

Acknowledgments: The authors express gratitude to PT. ASABA Surveying Division (Indonesia) for providing TLS instrument support and to PT. Geotronix Indonesia for providing a drone Lidar instrument during this research. Appreciation is also extended to Akram Sripandam, Dhani Yudi P, Arsa Faiz N, Iqbal Hanun A, and other students from the Vocational College, Gadjah Mada University, for their invaluable assistance in data acquisition and processing. Additionally, thanks are given to the Vocational College for supplying computational PCs during data processing and to the Balai Pelestarian Cagar Budaya (BPCB) for granting on-site permission and providing on-site supporting facilities.

Conflicts of Interest: The authors declare no conflicts of interest.

References

1. Emeralda, M.I. The Advantages of Prambanan Temple Existence and Its Conservation. *J. Bus. Hosp. Tour.* **2015**, *1*, 15. [CrossRef]
2. Khairunnisa, S.A.; Hidayat, T.; Orchiston, W.; Nikeu, N. Astronomical Aspects of the Prambanan Temple in Central Java, Indonesia. In *Exploring the History of Southeast Asian Astronomy*; Orchiston, W., Vahia, M.N., Eds.; Historical & Cultural Astronomy; Springer International Publishing: Cham, Switzerland, 2021; pp. 487–502, ISBN 978-3-030-62776-8.
3. de Casparis, J.G. *Prasasti Indonesia II; Selected Inscriptions from 7th to the 9th Century AD*; Masa Baru: Bandung, Indonesia, 1956.
4. Jordaan, R.E. *In Praise of Prambanan: Dutch Essays on The Lord Jonggrang Temple Complex*; Brill: Leiden, The Netherlands, 1996; ISBN 978-90-04-26042-9.
5. Tanudirjo, D.A. Pemugaran Kembali Candi Siwa Pascagempa 2006: Perspektif Arkeologi. *Bul. Narasimha* **2011**, *4*, 15–22.

6. Ohsumi, T.; Baba, K. Field Investigation on the Damage of Prambanan Temple, Housing and Infrastructure Caused by Earthquake in Central Java, Indonesia. *Proc. JSCE Earthq. Eng. Symp.* **2007**, *29*, 50–59. [CrossRef]
7. Herwindo, R.P. Candi Prambanan dalam Perspektif Arsitektur. In Proceedings of the Diskusi dan Pameran: Kompleks Candi Prambanan Sebagai Warisan Umat Manusia; Universitas Katholik Parahyangan: Jakarta, Indonesia, 2010; pp. 1–16.
8. Herwindo, R.P. *Eksistensi Candi: Sebagai Karya Agung Arsitektur Indonesia di Asia Tenggara*; PT Kanisius: Yogyakarta, Indonesia, 2018; ISBN 979-21-5517-1.
9. Setyastuti, A. Belajar dari Kearifan Lokal Nenek Moyang dalam Rekayasa Lahan dan Pembangunan Candi Prambanan. *Bul. Narasimha* **2011**, *4*, 10–14.
10. Ayuati, M.S. Studi Kelayakan Candi Perwara Deret I No. 5 Bagian dari Upaya Pelestarian Candi Prambanan. *Bul. Narasimha* **2019**, *12*, 35–43.
11. Setyastuti, A. Daya Dukung Fisik Zona 1 Candi Prambanan. *Bul. Narasimha* **2010**, *3*, 32–45.
12. Atmadi, P. *Some Architectural Design Principles of Temples in Java: A Study Through the Buildings Projection on the Reliefs of Borobudur Temple*, 2nd ed.; Gadjah Mada University Press: Yogyakarta, Indonesia, 1988; ISBN 979-420-085-9.
13. Datta, K. Relational Aspects of Hindu Temple Architecture Design: The Case of Candi Siwa & Lingaraja Temple. In Proceedings of the Conference Proceedings-International Conference on Built Environment, Science, and Technology (ICON-BEST 2021), Virtual, 20–21 February 2021; p. 122.
14. Martinus, A.; Herwindo, R.P. The Comparative Study on Architectural Typo-Morphology of Borobudur-Prambanan Temple and Angkor Wat, Case Study on Mass Order, Floor Plan, Figure and Ornaments. *Ris. Arsit. RISA* **2018**, *2*, 335–359. [CrossRef]
15. Sardar, D.; Kulkarni, S.Y. Role of Fractal Geometry in Indian Hindu Temple Architecture. *Int. J. Eng. Res. Technol.* **2015**, *V4*, IJERTV4IS050709. [CrossRef]
16. Saelee, C.; Riyaprao, O.; Komonjinda, S.; Sriboonrueang, K. An Archaeoastronomical Investigation of Vaastu Shastra Principles (Vedic Architecture) Implemented in the City Planning of Ancient Chiang Mai. In *Exploring the History of Southeast Asian Astronomy*; Orchiston, W., Vahia, M.N., Eds.; Historical & Cultural Astronomy; Springer International Publishing: Cham, Switzerland, 2021; pp. 461–485, ISBN 978-3-030-62776-8.
17. Muryamto, R.; Taftazani, M.I.; Yulaikhah, Y.; Cahyono, B.K.; Prasidya, A.S. Development and Definition of Prambanan Temple Deformation Monitoring Control Points. *J. Geospat. Inf. Sci. Eng.* **2019**, *1*, 81–86. [CrossRef]
18. Adrisijanti, I.; Putranto, A.; Ngesti, V. Site Conservation Assesment Report: Prambanan Temple Compound Indonesia. 2011. Available online: http://ghn.globalheritagefund.org/uploads/documents/document_1944.pdf (accessed on 28 June 2021).
19. Suryolelono, K.B. Candi Prambanan Pasca Gempa Bumi. *Forum Tek. Sipil* **2007**, *XVII*, 594–603.
20. Tsuji, T.; Yamamoto, K.; Matsuoka, T.; Yamada, Y.; Onishi, K.; Bahar, A.; Meilano, I.; Abidin, H.Z. Earthquake Fault of the 26 May 2006 Yogyakarta Earthquake Observed by SAR Interferometry. *Earth Planets Space* **2009**, *61*, e29–e32. [CrossRef]
21. Abidin, H.Z.; Andreas, H.; Meilano, I.; Gamal, M.; Gumilar, I.; Abdullah, C.I. Deformasi Koseismik Dan Pascaseismik Gempa Yogyakarta 2006 Dari Hasil Survei GPS. *Indones. J. Geosci.* **2009**, *4*, 275–284. [CrossRef]
22. Selvaggi, I.; Dellapasqua, M.; Franci, F.; Spangher, A.; Visintini, D.; Bitelli, G. 3D Comparison Towards a Comprehensive Analysis of a Building in Cultural Heritage. *Int. Arch. Photogramm. Remote Sens. Spat. Inf. Sci.* **2018**, *XLII–2*, 1061–1066. [CrossRef]
23. Dore, C.; Murphy, M. Current State of the Art Historic Building Information Modelling. *Int. Arch. Photogramm. Remote Sens. Spat. Inf. Sci.* **2017**, *XLII-2/W5*, 185–192. [CrossRef]
24. Barontini, A.; Alarcon, C.; Sousa, H.S.; Oliveira, D.V.; Masciotta, M.G.; Azenha, M. Development and Demonstration of an HBIM Framework for the Preventive Conservation of Cultural Heritage. *Int. J. Archit. Herit.* **2021**, *16*, 1451–1473. [CrossRef]
25. Bruno, N.; Roncella, R. HBIM for Conservation: A New Proposal for Information Modeling. *Remote Sens.* **2019**, *11*, 1751. [CrossRef]
26. Oreni, D.; Brumana, R.; Della Torre, S.; Banfi, F.; Barazzetti, L.; Previtali, M. Survey Turned into HBIM: The Restoration and the Work Involved Concerning the Basilica Di Collemaggio after the Earthquake (L'Aquila). *ISPRS Ann. Photogramm. Remote Sens. Spat. Inf. Sci.* **2014**, *II–5*, 267–273. [CrossRef]
27. Jouan, P.; Hallot, P. Digital Twin: A HBIM-Based Methodology to Support Preventive Conservation of Historic Assets through Heritage Significance Awareness. *Int. Arch. Photogramm. Remote Sens. Spat. Inf. Sci.* **2019**, *XLII-2/W15*, 609–615. [CrossRef]
28. López, F.; Lerones, P.; Llamas, J.; Gómez-García-Bermejo, J.; Zalama, E. A Review of Heritage Building Information Modeling (H-BIM). *Multimodal Technol. Interact.* **2018**, *2*, 21. [CrossRef]
29. Murtiyoso, A.; Grussenmeyer, P.; Suwardhi, D.; Awalludin, R. Multi-Scale and Multi-Sensor 3D Documentation of Heritage Complexes in Urban Areas. *ISPRS Int. J. Geo Inf.* **2018**, *7*, 483. [CrossRef]
30. Del Pozo, S.; Rodríguez-Gonzálvez, P.; Sánchez-Aparicio, L.J.; Muñoz-Nieto, A.; Hernández-López, D.; Felipe-García, B.; González-Aguilera, D. Multispectral Imaging in Cultural Heritage Conservation. *Int. Arch. Photogramm. Remote Sens. Spat. Inf. Sci.* **2017**, *XLII-2/W5*, 155–162. [CrossRef]
31. Chekole, S.D. Surveying with GPS, Total Station, and Terresterial Laser Scanner: A Comparative Study. Master's Thesis, Royal Institute of Technology (KTH), Stockholm, Sweden, 2014.

32. Jacobs, G. High Definition Surveying and Laser Scanning. *GeoInformatics* **2011**, *14*, 28–34. Available online: https://www.proquest.com/openview/4f01b6101ef02e065c811f759be022d2/1?pq-origsite=gscholar&cbl=178200 (accessed on 3 March 2022).
33. Monego, M.; Fabris, M.; Menin, A.; Achilli, V. 3-D Survey Applied to Industrial Archaeology by TLS Methodology. *Int. Arch. Photogramm. Remote Sens. Spat. Inf. Sci.* **2017**, *XLII-5/W1*, 449–455. [CrossRef]
34. Pocobelli, D.P.; Boehm, J.; Bryan, P.; Still, J.; Grau-Bové, J. BIM for Heritage Science: A Review. *Herit Sci* **2018**, *6*, 30. [CrossRef]
35. Petrie, G.; Toth, C.K. Terrestrial Laser Scanners. In *Topographic Laser Ranging and Scanning: Principles and Processing*; Taylor & Francis, CRC Press: Boca Raton, FL, USA, 2018; pp. 29–88, ISBN 978-1-4987-7227-3.
36. Quintero, M.S.; Genechten, B.V.; Bruyne, M.D.; Ronald, P.; Hankar, M.; Barnes, S. *Theory and Practice on Terrestrial Laser Scanning: Training Material Based on Practical Applications*; Learning Tools for Advanced Three-Fimensional Surveying in Risk Awareness Project (3DRiskMapping); Universidad Politecnica de Valencia: Valencia, Spain, 2008.
37. Jo, Y.; Hong, S. Three-Dimensional Digital Documentation of Cultural Heritage Site Based on the Convergence of Terrestrial Laser Scanning and Unmanned Aerial Vehicle Photogrammetry. *ISPRS Int. J. Geo Inf.* **2019**, *8*, 53. [CrossRef]
38. Baik, A.; Alitany, A.; Boehm, J.; Robson, S. Jeddah Historical Building Information Modelling "JHBIM"–Object Library. *ISPRS Ann. Photogramm. Remote Sens. Spat. Inf. Sci.* **2014**, *II–5*, 41–47. [CrossRef]
39. Murtiyoso, A.; Grussenmeyer, P.; Freville, T. Close Range UAV Accurate Recording and Modeling of St-Pierre-Le-Jeune Neo-Romanesque Church in Strasbourg (France). *Int. Arch. Photogramm. Remote Sens. Spat. Inf. Sci.* **2017**, *XLII-2/W3*, 519–526. [CrossRef]
40. Fang, J.; Zhang, Y.; Zhang, Y.; Guo, H.; Sun, Z. High-Definition Survey of Architectural Heritage Fusing Multisensors—The Case of Beamless Hall at Linggu Temple in Nanjing, China. *Sensors* **2022**, *22*, 3369. [CrossRef]
41. Khalloufi, H.; Azough, A.; Ennahnahi, N.; Kaghat, F.Z. Low-Cost Terrestrial Photogrammetry for 3D Modeling of Historic Sites: A Case Study of The Marinids' Royal Necropolis City of Fez, Morocco. *Mediterr. Archaeol. Archaeom.* **2020**, *20*, 257–272. [CrossRef]
42. Teppati Losè, L.; Chiabrando, F.; Giulio Tonolo, F. Documentation of Complex Environments Using 360° Cameras. The Santa Marta Belltower in Montanaro. *Remote Sens.* **2021**, *13*, 3633. [CrossRef]
43. Andaru, R.; Cahyono, B.K.; Riyadi, G.; Istarno; Djurdjani; Ramadhan, G.R.; Tuntas, S. The Combination of Terrestrial LiDAR and UAV Photogrammetry for Interactive Architectural Heritage Visualization Using Unity 3D Game Engine. *Int. Arch. Photogramm. Remote Sens. Spat. Inf. Sci.* **2019**, *XLII-2/W17*, 39–44. [CrossRef]
44. Guarnieri, A.; Fissore, F.; Masiero, A.; Vettore, A. From TLS Survey to 3D Solid Modeling for Documentation of Built Heritage: The Case Study of Porta Savonarola in Padua. *Int. Arch. Photogramm. Remote Sens. Spat. Inf. Sci.* **2017**, *XLII-2/W5*, 303–308. [CrossRef]
45. Stanga, C.; Banfi, F.; Roascio, S. Enhancing Building Archaeology: Drawing, UAV Photogrammetry and Scan-to-BIM-to-VR Process of Ancient Roman Ruins. *Drones* **2023**, *7*, 521. [CrossRef]
46. Abate, D.; Sturdy-Colls, C. A Multi-Level and Multi-Sensor Documentation Approach of the Treblinka Extermination and Labor Camps. *J. Cult. Herit.* **2018**, *34*, 129–135. [CrossRef]
47. Murtiyoso, A.; Suwardhi, D.; Grussenmeyer, P.; Fadilah, W.A.; Fauzan, K.N.; Trisyanti, S.W.; Brahmantara; Macher, H. Heritage Documentation and Knowledge Transfer: A Report on the CIPA Tropical School in Candi Sewu (Indonesia). *Int. Arch. Photogramm. Remote Sens. Spat. Inf. Sci.* **2021**, *XLVI-M-1–2021*, 493–497. [CrossRef]
48. Donato, E.; Giuffrida, D. Combined Methodologies for the Survey and Documentation of Historical Buildings: The Castle of Scalea (CS, Italy). *Heritage* **2019**, *2*, 2384–2397. [CrossRef]
49. Cahyandaru, N.; Brahmantara, B. Development of Digital Monitoring Methodology. *J. Konserv. Cagar Budaya* **2007**, *1*, 24–26. [CrossRef]
50. Suwardhi, D.; Menna, F.; Remondino, F.; Hanke, K.; Akmalia, R. Digital 3D Borobudur–Integration of 3D Surveying and Modeling Techniques. *Int. Arch. Photogramm. Remote Sens. Spat. Inf. Sci.* **2015**, *XL-5/W7*, 417–423. [CrossRef]
51. Fitri, A.; Sapta Widartono, B. Utilization of Aerial Photograph for Spasial Data Using Quadcopter (Ijo Temple Complex, District Prambanan, Yogyakarta). In Proceedings of the lst International Cohference on Geography and Education (ICGE 2016), Malang, Indonesia, 29 October 2016.
52. Murtiyoso, A.; Grussenmeyer, P.; Suwardhi, D. Technical Considerations in Low-Cost Heritage Documentation (Candi Sari-Case Study). *Int. Arch. Photogramm. Remote Sens. Spat. Inf. Sci.* **2019**, *XLII-2/W17*, 225–232. [CrossRef]
53. Santosa, H.; Yudono, A.; Adhitama, M.S. The Digital Management System of the Tangible Culture Heritage for Enhancing Historic Building Governance in Malang, Indonesia. *IOP Conf. Ser. Earth Environ. Sci.* **2021**, *738*, 012056. [CrossRef]
54. Surpi, N.K. Śivagrha (Prambanan Temple) as an Archetype of Hindu Theology in Nusantara (An Endeavor to Discover Hindu Theological Knowledge through Ancient Temple Heritage). *Anal. J. Soc. Sci. Relig.* **2020**, *5*, 107–122. [CrossRef]
55. BP3-Yogyakarta. *Studi Teknis Prambanan*; Balai Pelestarian Peninggalan Purbakala (BP3)-Yogyakarta: Yogyakarta, Indonesia, 2007.
56. Shodiq, A.M.; Widjajanti, N. Deformasi Horisontal Aspek Geometrik Candi Prambanan Sebelum dan Sesudah Gempa Yogyakarta Tahun 2006. Undergraduate Thesis, Universitas Gadjah Mada, Yogyakarta, Indonesia, 2015.

57. Sari, S.P.I. Penentuan Tinggi Titik Pantau Candi Prambanan dengan Metode Sipat Datar Menggunakan Hitung Perataan Metode Parameter Dengan Variasi Nilai Bobot. Undergraduate Thesis, Program Studi Sarjana Teknik Geodesi, Fakultas Teknik, Universitas Gadjah Mada, Yogyakarta, Indonesia, 2019.
58. Widyaningsih, L. Penentuan Koordinat 3D pada Titik Pantau Deformasi Badan Candi Prambanan Dengan Hitung Perataan. Undergraduate Thesis, Program Studi Sarjana Teknik Geodesi, Fakultas Teknik, Universitas Gadjah Mada, Yogyakarta, Indonesia, 2019.
59. Arrofiqoh, E.N.; Muryamto, R.; Afiyanti, D.; Azizah, S.C.; Kresnawan, D.S.; Fabiola, A.N. Pemanfaatan UAV Dengan Sensor Kamera Dan Lidar Untuk Pemetaan Situs Cagar Budaya Kawasan Candi Prambanan. *Geoid* **2022**, *17*, 176. [CrossRef]
60. Alidoost, F.; Arefi, H. An Image-Based Technique for 3D Building Reconstruction Using Multi-View UAV Images. *Int. Arch. Photogramm. Remote Sens. Spat. Inf. Sci.* **2015**, *XL-1/W5*, 43–46. [CrossRef]
61. Altman, S.; Xiao, W.; Grayson, B. Evaluation of Low-Cost Terrestrial Photogrammetry for 3D Reconstruction of Complex Buildings. *ISPRS Ann. Photogramm. Remote Sens. Spat. Inf. Sci.* **2017**, *IV-2/W4*, 199–206. [CrossRef]
62. Elkhrachy, I. Modeling and Visualization of Three Dimensional Objects Using Low-Cost Terrestrial Photogrammetry. *Int. J. Archit. Herit.* **2020**, *14*, 1456–1467. [CrossRef]
63. Han, Y.; Zhou, S.; Xia, P.; Zhao, Q. Research on Fine 3D Modeling Technology of Tall Buildings Based on UAV Photogrammetry. In Proceedings of the 2022 3rd International Conference on Geology, Mapping and Remote Sensing (ICGMRS), Zhoushan, China, 22–24 April 2022; pp. 349–353.
64. Barazzetti, L.; Previtali, M.; Roncoroni, F. 3D Modeling with 5k 360° Videos. *Int. Arch. Photogramm. Remote Sens. Spat. Inf. Sci.* **2022**, *XLVI-2/W1-2022*, 65–71. [CrossRef]
65. Herban, S.; Costantino, D.; Alfio, V.S.; Pepe, M. Use of Low-Cost Spherical Cameras for the Digitisation of Cultural Heritage Structures into 3D Point Clouds. *J. Imaging* **2022**, *8*, 13. [CrossRef]
66. Marcos-González, D.; Álvaro-Tordesillas, A.; López-Bragado, D.; Martínez-Vera, M. Fast and Accurate Documentation of Architectural Heritage with Low-Cost Spherical Panoramic Photographs from 360 Cameras. *Int. Arch. Photogramm. Remote Sens. Spat. Inf. Sci.* **2023**, *XLVIII-M-2–2023*, 1007–1011. [CrossRef]
67. Sun, Z.; Zhang, Y. Accuracy Evaluation of Videogrammetry Using a Low-Cost Spherical Camera for Narrow Architectural Heritage: An Observational Study with Variable Baselines and Blur Filters. *Sensors* **2019**, *19*, 496. [CrossRef]
68. Iglhaut, J.; Cabo, C.; Puliti, S.; Piermattei, L.; O'Connor, J.; Rosette, J. Structure from Motion Photogrammetry in Forestry: A Review. *Curr For. Rep* **2019**, *5*, 155–168. [CrossRef]
69. Westoby, M.J.; Brasington, J.; Glasser, N.F.; Hambrey, M.J.; Reynolds, J.M. 'Structure-from-Motion' Photogrammetry: A Low-Cost, Effective Tool for Geoscience Applications. *Geomorphology* **2012**, *179*, 300–314. [CrossRef]
70. Pfeifer, N.; Briese, C. Laser Scanning-Principles and Applications. In Proceedings of the GeoSiberia 2007-International Exhibition and Scientific Congress; European Association of Geoscientists & Engineers, Novosibirsk, Russia, 25 April 2007; p. cp-59.
71. Reshetyuk, Y. Self-Calibration and Direct Georeferencing in Terrestrial Laser Scanning. Ph.D. Thesis, Royal Institute of Technology (KTH), Stockholm, Sweden, 2009.
72. Wujanz, D. Construction Site Monitoring Based on Laser Scanning Data. In *Laser Scanning: An Emerging Technology in Structural Engineering*; International society for photogrammetry and remote sensing (ISPRS) book series; CRC Press/Balkema: Leiden, The Netherlands, 2020; pp. 231–246, ISBN 978-1-138-49604-0.
73. Lague, D.; Brodu, N.; Leroux, J. Accurate 3D Comparison of Complex Topography with Terrestrial Laser Scanner: Application to the Rangitikei Canyon (N-Z). *ISPRS J. Photogramm. Remote Sens.* **2013**, *82*, 10–26. [CrossRef]
74. DiFrancesco, P.-M.; Bonneau, D.; Hutchinson, D.J. The Implications of M3C2 Projection Diameter on 3D Semi-Automated Rockfall Extraction from Sequential Terrestrial Laser Scanning Point Clouds. *Remote Sens.* **2020**, *12*, 1885. [CrossRef]
75. Georgantas, A.; Brédif, M.; Pierrot-Desseilligny, M. An Accuracy Assessment of Automated Photogrammetric Techniques for 3D Modeling of Complex Interiors. *Int. Arch. Photogramm. Remote Sens. Spat. Inf. Sci.* **2012**, *XXXIX-B3*, 23–28. [CrossRef]
76. Koutsoudis, A.; Vidmar, B.; Ioannakis, G.; Arnaoutoglou, F.; Pavlidis, G.; Chamzas, C. Multi-Image 3D Reconstruction Data Evaluation. *J. Cult. Herit.* **2014**, *15*, 73–79. [CrossRef]
77. Morgan, J.A.; Brogan, D.J.; Nelson, P.A. Application of Structure-from-Motion Photogrammetry in Laboratory Flumes. *Geomorphology* **2017**, *276*, 125–143. [CrossRef]
78. Moyano, J.; Nieto-Julián, J.E.; Bienvenido-Huertas, D.; Marín-García, D. Validation of Close-Range Photogrammetry for Architectural and Archaeological Heritage: Analysis of Point Density and 3D Mesh Geometry. *Remote Sens.* **2020**, *12*, 3571. [CrossRef]
79. Kazhdan, M.; Hoppe, H. Screened Poisson Surface Reconstruction. *ACM Trans. Graph.* **2013**, *32*, 1–13. [CrossRef]
80. Alshawabkeh, Y.; Baik, A. Integration of Photogrammetry and Laser Scanning for Enhancing Scan-to-HBIM Modeling of Al Ula Heritage Site. *Herit. Sci.* **2023**, *11*, 147. [CrossRef]
81. Rocha, G.; Mateus, L.; Fernández, J.; Ferreira, V. A Scan-to-BIM Methodology Applied to Heritage Buildings. *Heritage* **2020**, *3*, 47–67. [CrossRef]

82. Nursyahirah, A.F.; Yusoff, A.R.; Ismail, Z.; Majid, Z. Comparing the Performance of Point Cloud Registration Methods for Landslide Monitoring Using Mobile Laser Scanning Data. *Int. Arch. Photogramm. Remote Sens. Spat. Inf. Sci.* **2018**, *XLII-4/W9*, 11–21. [CrossRef]
83. BP3-Yogyakarta. *Membangun Kembali Prambanan*; Balai Pelestarian Peninggalan Purbakala (BP3)-Yogyakarta: Yogyakarta, Indonesia, 2009; p. 124.
84. Grussenmeyer, P.; Hanke, K.; Streilein, A. Architectural Photogrammetry: Basic Theory, Procedures, Tools. In *Digital Photogrammetry*; Klasser, M., Egels, Y., Eds.; Taylor & Francis: Abingdon, UK, 2002; pp. 300–339.
85. Adamopoulos, E.; Rinaudo, F. Combining Multiband Imaging, Photogrammetric Techniques, and FOSS GIS for Affordable Degradation Mapping of Stone Monuments. *Buildings* **2021**, *11*, 304. [CrossRef]
86. Huang, X.; Mei, G.; Zhang, J. Cross-Source Point Cloud Registration: Challenges, Progress and Prospects. *Neurocomputing* **2023**, *548*, 126383. [CrossRef]
87. Luhmann, T.; Robson, S.; Kyle, S.; Boehm, J. *Close-Range Photogrammetry and 3D Imaging*; de Gruyter: Berlin, Germany, 2019.